Thesis for the degree of Doctor of Philosophy in
Thermo and Fluid Dynamics

Experimental and numerical investigations of underhood flow for vehicle thermal management

RANDI FRANZKE

Department of Mechanics and Maritime Sciences
CHALMERS UNIVERSITY OF TECHNOLOGY
Göteborg, Sweden 2021

Experimental and numerical investigations of underhood flow for vehicle thermal management
RANDI FRANZKE
ISBN 978-91-7905-585-1

Doktorsavhandlingar vid Chalmers tekniska högskola
Ny serie nr. 5052
ISSN 0346-718X

Department of Mechanics and Maritime Sciences
Chalmers University of Technology
SE–412 96 Göteborg
Sweden
Telephone: +46 (0)31–772 1000

Chalmers Reproservice
Göteborg, Sweden 2021

" Science [...] is a method for asking awkward questions and subjecting them to a reality-check, thus avoiding the human tendency to believe whatever makes us feel good."

– Sir Terry Pratchett

Experimental and numerical investigations of underhood flow for vehicle thermal management

Randi Franzke
Department of Mechanics and Maritime Sciences
Chalmers University of Technology

Abstract

Electrified vehicles are an essential part in reducing emissions from the transportation sector. Their development comes with a variety of new challenges. Most of them revolve around the energy efficiency of the vehicles as it directly relates to the range that can be covered with one charge. In the area of vehicle thermal management, this means that the focus shifts from a pure cooling perspective towards providing a thermal environment in which the electric power components can operate most efficiently. As the required amount of cooling air through the front is lower than in conventional combustion vehicles, an additional benefit can be gained from smaller front openings that reduce the aerodynamic drag. However, this requires a deeper knowledge of the flow physics in the underhood environment in order to utilise the available cooling air efficiently.
Computational Fluid Dynamics (CFD) is an important tool for the investigation of the underhood flow, since it gives the possibility to look at the flow field even in areas where measurement equipment cannot reach. In the first part of this work, the focus is on the simulation of the axial cooling fan. Different methods to simulate an axial cooling fan were compared to each other and to experimental data that was acquired using Laser-Doppler-Anemometry. The commonly used Multiple Reference Frame approach was shown not to be suitable for investigating underhood flow, as the stationary blades leave an imprint on the wake flow. In addition, inhomogeneous temperature distributions experienced an unphysical rotation due to the switch in reference frame. These issues do not occur with the Rigid Body Motion approach, and the simulation results compared well to the measurements.
In the second part of this project, it was investigated how the flow downstream of a fan is affected by different components placed up- and downstream. A simplified underhood rig was designed and constructed to provide a controlled, vehicle-like environment for the measurements and simulations. Two front designs, representative of a hybrid and a battery electric vehicle, were utilised and it could be shown that the upper grille opening that is missing in the battery electric vehicle configuration has a visible impact on the flow field downstream of the fan. Simulating the same configurations in CFD showed some differences to the experimental data. For a second cooling fan, the results were well matched.

Keywords: Vehicle thermal management, Axial fan, Underhood flow, Cooling flow, CFD, MRF, RBM, Laser-Doppler anemometry, Simplified underhood environment

Acknowledgements

This project would not have been possible without the financial support that was granted by the funding through the Swedish Energy Agency within the framework *Fordonsstrategisk forskning och innovation (FFI)* and the Volvo Car Group, which I gratefully acknowledge.

Furthermore, I would like to thank my examiner and supervisor Prof. Simone Sebben for her guidance and thorough editing of my papers throughout this project. I would also like to thank my co-supervisors Emil Willeson and Alexander Broniewicz for their support and helping me to focus on my work. Tore Bark I would like to thank for always having an open ear when I needed to discuss basic and not-so-basic fluid mechanics.

Second, I would like to thank my colleagues in the Thermal Efficiency group, the PVT workshop and other colleagues all over Volvo that provided me with helping hands and support when I needed it. Special thanks go to Leif Steinar, Brian Fechtner and Samuel Utbult.

My former and present colleagues at VEAS I would like to thank for providing a great work environment and counterbalance to stressful work days. It is a huge privilege to work with your friends and I will miss our office discussions, coffee breaks, climbing sessions and Friday beers (though we'll hopefully be keeping up the latter!). Sonja, thank you for all the support, care and coffee you provided us with!

Last but not least, I want to thank my family for all their unconditional support and encouragement along the way. And thank you, Pär, for being part of most of (if not all) the best moments during the past years and lifting me up when needed.

List of included papers

This thesis consists of the following papers. References to the papers will be made using Roman numerals.

I Franzke, R., Sebben, S., *Validation of Different Fan Modelling Techniques in Computational Fluid Dynamics*. Proceedings of the 21st Australasian Fluid Mechanics Conference, Adelaide, 2018.

II Franzke, R., Sebben, S., Bark, T. and Willeson, E., *Evaluation of the Multiple Reference Frame Approach for the Modelling of an Axial Cooling Fan*. Energies, 2019.

III Franzke, R., Sebben, S. and Willeson, E., *Experimental investigation of the air flow in a simplified underhood environment*. Accepted for publication in: IMechE Part D: Journal of Automobile Engineering, 2021.

IV Franzke, R., Sebben, S. and Willeson, E., *Numerical investigation of the air flow in a simplified underhood environment*. Submitted to: International Journal of Automotive Technology, 2021.

The author of this thesis was responsible for conducting the experiments and simulations, as well as analysing the results and writing the papers. The co-authors contributed with supervision, technical discussions and review of the manuscripts.

Other relevant publication not included in the thesis:

(a) Franzke, R., Svensson, R., Thiringer, T., Willeson, E., Grunditz, E., Broniewicz, A., *Measurements and CFD Modeling of Temperatures in the Engine Compartment of a Hybrid Electric Vehicle*. Proceedings of the 2017 Vehicle Power and Propulsion Conference, Belfort (France), 2017.

The author of this thesis was responsible for conducting the simulations, analysing the results and writing the manuscript with the assistance of the co-authors.

The experimental part was conducted by Svensson and Willeson. Thiringer and Grunditz provided boundary conditions for the electric components modelled, and their expertise in electric machines. All co-authors contributed with supervision, technical discussions and the review of the manuscript.

Table of Contents

Nomenclature

Symbol	Unit	Description
d,D	m	Diameter
f	1/s	Frequency
k	m^2/s^2	Turbulent kinetic energy
l,L	m	Length
$\dot{m}$	kg/s	Mass flow rate
P_i	kg/m^4	Porous inertia resistance tensor
P_v	kg/m^3s	Porous viscous resistance tensor
$\boldsymbol{r}$	m	Radial position
R	m	Outer radius
u_τ	m/s	Friction velocity
$\boldsymbol{u}$	m/s	Velocity vector
x,y,z	m	Position in global reference frame
y^+	–	Dimensionless wall distance
ε	m^2/s^3	Turbulent dissipation rate
λ	nm	Wave length
ω	1/s	Specific turbulent dissipation rate
$\boldsymbol{\omega}$	rpm	Rotational vector

Abbreviations

BEV	Battery Electric Vehicle
BSA	Burst Spectrum Analyser
CFD	Computational Fluid Dynamics
CFL	Courant Friedrichs Lewis (number)
DES	Detached Eddy Simulation
DDES	Delayed Detached Eddy Simulation
HEV	Hybrid Electric Vehicle
IDDES	Improved Delayed Detached Eddy Simulation
LDA	Laser Doppler Anemometry
LES	Large Eddy Simulation
MRF	Multiple or Moving Reference Frame
MWT	Model Wind Tunnel
PVT	*Personvagnars Vindtunnel* (full-scale wind tunnel at Volvo Cars)
PWM	Pulse Width Modulation
RANS	Reynolds-averaged Navier Stokes
RBM	Rigid Body Motion
SGS	Sub-grid Scale

1 Introduction

1.1 Background

In recent years, the sales of vehicles with various degrees of electrification have been on the rise. From the start of this project in 2016 the percentage of electrified vehicles amongst new registrations in Sweden has increased from 7 % to 55 % in June 2021 [1]. This trend can be observed in most industrialised countries and is a combined effect of an increased environmental consciousness amongst customers to reduce CO_2 emissions, governmental support and improved technical maturity of electrified vehicles over a large range of manufacturers.

With the transition away from combustion engines, the thermal environment in the underhood region of a passenger vehicle is drastically changing. Instead of dealing with very high temperatures and a large amount of thermal mass, the focus in electric vehicles is on providing conditions in which the power components can operate in their most efficient way, as well as preventing unwanted heat loss or pick-up by the cooling system. The reduced need for external cooling air also makes smaller inlet openings possible. Given that the cooling air flow through the underhood accounts for up to 10 % of the overall aerodynamic drag [2], reducing the front inlet openings will have a positive effect on the energy efficiency and, hence, the driving range of the vehicle. However, this smaller amount of external cooling air needs to be appropriately guided to make the most use of it.

Parallel to this, the trend within the industry towards virtual development continues. Increased computational resources and continuously improving tools allow for a more accurate assessment of new designs at early stages of the development of a vehicle. This reduces the amount of physical test objects and shortens the time to market. However, it requires the employed computational methods to provide accurate results. In vehicle thermal management, an important tool to simulate the flow field and heat transfer is Computational Fluid Dynamics (CFD). For vehicles with an internal combustion engine, it has often been sufficient to validate these simulations with temperature measurements for high load cases, in order to stay

within a certain range, depending on the component, in order to prevent damages. In the development of electric vehicles, new heat sources need to be taken into consideration and other dimensioning cases become relevant, such as fast charging. Hence, the numerical prediction of the underhood flow gains on importance and needs to be validated as well.

A pre-study to this work, that was performed at Volvo Cars in cooperation with the department of Energy of Environment (E2) at Chalmers, showed that incorporating the components of the electric driveline as heat sources into a full vehicle simulation yielded good results (Paper (a)) [3]. However, it also revealed that the flow out of the cooling fan, and thereby the transport of the higher temperatures from the heat exchanger, was not captured accurately. These results led to the main focus of this project, which is the modelling of the main cooling fan and the performance of current state of the art simulation methods to capture the flow field downstream of the fan in different underhood installations.

1.2 Previous works

This thesis combines the areas of experimentally investigating underhood flow and validation of numerical methods for their accuracy in predicting it.

The aspect of measuring underhood flow has been of interest already in the early 1990s, before electric vehicles were seriously discussed as an alternative to combustion engines. Cogotti and Berneburg [4, 5] investigated the possibilities of measuring the flow in the engine bay of an Opel Vectra. Together with Dantec Dynamics they developed a Laser-Doppler-Anemometry (LDA) probe that measures all three components of the velocity vector, and mapped the flow field directly downstream of the fan and around the lambda sensor. The main challenge was the accessibility to the measurement areas in a full-scale passenger car due to the tight packaging in the engine bay. Williams et al. [6] used a vehicle with a transparent hood to perform flow visualisation in a water tow tank. However, only qualitative information of the area visible through the hood could be obtained. The most feasible component along the cooling channel to obtain flow measurements in a vehicle installation from is the radiator. Here, measurements with vane [5] or hot-wire anemometers [7], as well as pressure probes [8] can give quantitative information about the amount and distribution of the cooling flow entering the underhood region. Downstream of the axial cooling fan, the proximity to other components makes measurements more difficult to achieve in a complete vehicle installation.

More recently, Khaled et al. [9, 10] developed a simplified underhood geometry to experimentally study the effect different distances between an engine mock-up and

a cooling module have on the underhood flow and the performance of the cooling package. The same rig was later used by Faraj et al. [11] to optimise the packing in the underhood for cooling drag. In their study, the aerodynamic drag could be reduced by 1.4 % by adjusting the space between the cooling module and the simplified engine geometry. Karlsson and Etemad [12] combined the benefits of a plenum rig with a generic underhood box to investigate the installation effect on noise generated by an array of automotive cooling fans.

The usage of simplified underhood rigs is already a well established praxis within the validation of numerical methods for buoyancy driven flows, that occur during thermal soak [13, 14, 15]. The validation of forced convection simulations, due to ram air or the running fan, have not been reported in such a setting. Instead, so-called plenum rigs are often used for aerodynamic and -acoustic fan investigations of fan driven flow [16, 17]. These rigs are convenient as they give good access to the measurement area and allow to measure the flow field at different operating points by controlling the pressure rise over the fan [18, 19].

The possibility to vary the operating points makes plenum rigs an important part in providing validation data for CFD. One of the main focus areas in the past decades revolved around the validation of the Moving Reference Frame (MRF) approach, sometimes also referred to as Multiple Reference Frame method. This method offers cost-efficient simulation of the axial cooling fan without needing experimental input data as it was previously the case for 1 D fan models. Initial fan simulations performed by Moreau et al. [20] for one blade passage under the assumption of rotational symmetric boundary conditions showed good agreement with an experimentally obtained fan curve and against hot-wire measurements [21]. However, when including a stator to the set-up in later studies [22], the MRF model was found to underpredict the fan performance curve by 5-25 %. Similar numbers were reported by Gullberg et al. [23, 24], who in numerous studies between 2009 and 2014 investigated the limitations of the MRF method. The results showed that the fan curve could be predicted by steady-state simulations if the fan operates in axial condition. For radial and stall conditions, the MRF model could not match the experimentally obtained fan curve. The work of Gullberg [25] also included methods to mitigate these negative effects without having to switch to the unsteady, and hence more expensive, Sliding Mesh method. By comparing his numerical results to experimentally obtained fan curves, Gullberg [26] could show that a larger MRF region improves the prediction of the fan curve, and the pressure rise is with less than 1 % deviation from the experimental results in the axial flow range. Kobayashi et al. [27] came to the same conclusion and showed that an uneven flow behaviour induces an unphysical strain-rate at the MRF interfaces, which causes inaccuracies. In another study, Gullberg et al. [28] presented an approach that averaged the results from multiple blade positions and yielded an improvement in the prediction of the fan curve.

In contrast to previous research work, Gullberg et al. [29] also included an engine mock-up downstream and a radiator upstream of the fan in the plenum rig in order to validate the CFD methods for more realistic in- and outflow conditions. Rynell [17] numerically and experimentally evaluated the aerodynamics and -acoustics of an axial fan with a radiator mounted upstream of the rotor. The results from using advanced numerical methods (Sliding Mesh with IDDES turbulence modelling) agreed well with the acoustic measurements. Furthermore, the author stressed the importance of studying the fan in its installation, as they have a strong impact on the fan flow behaviour. Riesterer [30] investigated the temperature transfer through the fan region with the MRF method and compared the simulation results to flow and temperature data obtained from plenum rigs. Some deficiencies were noted and a modified MRF method proposed to balance the effect. Purely experimental studies on the installation effect have, amongst others, been performed by Gifford et al. [31] as well as Wen et al. [18] using plenum rigs.

1.3 Objectives and limitations

This project evaluates state of the art simulation methods for vehicle thermal management in terms of their ability to predict the flow field in the underhood environment for different installations. Its main objective is to improve the understanding of underhood flow physics and provide a comprehensive overview of the capabilities and limitations of current CFD methods.

In this thesis, the following research questions are discussed:

1. How do geometric factors up- and downstream of the cooling fan influence the air flow in the underhood environment?

2. How well is the flow behaviour downstream of the fan captured by current CFD methods?

3. Can the accuracy of CFD simulations be improved within affordable time-cost-constraints?

The work consists of both numerical and experimental studies. The measurements are performed under isothermal conditions, thus no heat sources are included in the physical set-ups. This is not seen as a strong limitation, as the prediction of the flow field, forced by the fan, is the focus of this thesis. To better understand the different influencing factors on the flow behaviour, the performed studies are limited to different test stands. The chosen set-ups provide a controlled environment, with gradually increasing complexity. Measurements in an actual vehicle are not part of the scope. It was also decided not to use a plenum-to-plenum rig, which limits the

amount of possible operation points of the fan. However, cases with and without external flow contribution were considered and the idling cases are regarded as particularly relevant, given that one of the thermal dimensioning cases for electric vehicles is fast charging.

1.4 Outline

This thesis starts out with a general description of the numerical and experimental methods used over the course of the project (Chapter 2). In Chapter 3, the different fan modelling approaches are compared to each other and validated with experimental data. Moreover, the transport of the temperature field through the MRF region is numerically investigated. Chapter 4 contains a detailed description of the simplified underhood environment that was designed to evaluate the influence of different inlet and blockage conditions. Furthermore, the experimental results from a variety of measurement configurations are presented and compared to different numerical simulations. Finally, the results are summarised and suggestions for possible future work are given in Chapter 5. An overview of the appended papers is provided in Chapter 6.

2 | Methodology

For this research project various numerical and experimental methods were used. In this chapter the fundamentals behind the employed methods are described in a more general matter, while the detailed procedures are discussed in the chapters dealing with the individual parts of the project.

2.1 Numerical methods

All simulations presented in this thesis were performed with the CFD software Simcenter StarCCM+ by Siemens [32]. Simcenter StarCCM+ is a finite volume solver that solves the governing flow equations (conservation of mass, momentum and energy) on a discretised grid. As direct numerical simulations (DNS) of turbulent flow are not feasible for industrial applications, additional assumptions have to be made to model the flow. One way is to time-averaging the governing equations, which leads to the Reynolds-averaged Navier-Stokes (RANS) equations. A second option is to apply spatial filters that allow to resolve the larger turbulent scales, while modelling the smaller ones. These approaches belong to the category of scale-resolving methods and will be briefly described here.

2.1.1 RANS-based models

In the Reynolds-averaged Navier-Stokes equations, the physical quantities are split into a time-averaged ($\overline{\phi}$) and a fluctuating (ϕ') component:

$$\phi(t) = \overline{\phi} + \phi'(t) \tag{2.1}$$

The governing equations in RANS formulation can be easily found in literature, e. g. [33], and are therefore not presented here. RANS models are available for steady and unsteady simulations. Steady-state RANS simulation can be either used on their own or as an initialisation for unsteady RANS, often referred to as URANS.

The resulting system of equations in RANS or URANS formulation is easy to solve numerically, but contains an additional term with the so-called Reynolds stresses. Hence, supplementary equations are needed to close the system of equations. The Reynolds-stress equation model (RSM) is sometimes used, which includes seven additional partial differential equations and therefore is computationally expensive. More efficient approaches are based on zero- to two-equation models and include properties of the turbulent flow.

Models based on different formulations of the two-equation k-ε approach are commonly used for underhood flow simulations [34, 15] and have been used for previous fan investigations in various formulations. These models include a transport equation for the turbulent kinetic energy k and turbulent dissipation rate ε. Moreau [20] and Henner et al. [22] used the Standard k-ε model, which was also initially used by Kohri et al. [19]. However, they found the RNG k-ε model to be more suitable for fan simulations, which was then used in a later study by Kobayashi et al. [27]. Gullberg [25] used the Realisable k-ε two-layer model, which has been used for parts of the work presented in this thesis.

2.1.2 Scale-resolving methods

Resolving the large turbulent length scales while modelling the small-scale fluctuations, is a step towards more physical representation of the flow. This method is called Large Eddy Simulation (LES) and is achieved by spatially filtering of the properties of the governing equations instead of using a time-averaging approach as for the RANS equations.

The cut-off width for the spacial filter in CFD is usually set to the grid size, as it would be pointless to filter for structures smaller than what can be resolved by the mesh itself [33]. The stresses originating from the turbulent scales that are smaller than the cut-off width are modelled with the so-called Sub-Grid Scale (SGS) models. The governing equations in LES formulation and an overview over common SGS models can, amongst others, be found in [33] or [35]. Even though only the large scale turbulence is resolved, the requirements on the spacial and temporal resolution can be substantial, which makes it a computationally expensive approach, especially in the near-wall regions of high Reynolds number flows. A few examples can be found in literature, where an LES was performed on a rotor-stator flow [36, 37, 38]. However, these examples are usually restricted to one or a few blade passages to keep the computational load manageable, hence an LES is not suitable to study installation effects on the underhood flow.

Hybrid approaches, such as the Detached Eddy Simulation (DES), try to breach the gap between RANS and Large Eddy Simulations. A DES combines the higher

accuracy of LES in the bulk flow with the lower computational requirements of URANS simulations in the near-wall region. This keeps the necessary amount of cells low and reduces the computational time in comparison to a full LES. The transition between the URANS and the LES regions is performed by shielding functions. Variations of the classical DES approach include the Delayed DES (DDES), which improves the switch between RANS and LES, and the Improved Delayed Eddy Simulation (IDDES), which includes a dependency of the sub-grid length scale on the wall distance and thereby allows for a thinner URANS region.

DES and IDDES have been successfully applied in numerical studies of thermal soak in a simplified engine bay rig [34] with the Spalart-Allmaras turbulence model in the URANS region close to the wall, as well as for a radial turbine by Lim et al. [39] using the SST k-ω model for closure in the URANS region. The same approach was used by Rynell [40] to simulate the aeroacoustics of an isolated automotive fan. For Paper IV the DDES model with the Elliptic-blending k-ε model has been primarily used. In addition, IDDES models with the one-equation Spalart-Allmaras [41] and the two-equation k-ω SST model [42] were used, to investigate the impact of the near-wall modelling in unsteady hybrid RANS-LES approaches. The Spalart-Allmaras model solves the transport equation for the modified diffusivity to determine the turbulent eddy viscosity. It is reported to show good results for attached boundary layer flow, such as around airfoils, but to give less accurate results in jet-like flow regions and complex recirculation areas [43]. The k-ω SST model is known for its good applicability in flow with adverse pressure gradients.

With increasing computational resources, DES, IDDES and other hybrid approaches can be expected to become more common methods in future industrial applications. However, they still require a carefully designed mesh to be robust and yield accurate results.

2.1.3 Mesh and near-wall modelling

The meshes used in the performed studies were created within the CFD software by first applying a surface wrapper to the respective region, followed by filling the computational domain with a volume mesh. The domain was split into multiple regions, one around the fan blades, one for the heat exchangers (when included), and one for the remaining domain. For the fan region an unstructured mesh with polyhedral cells was used. This is beneficial when creating a mesh around complex geometries [32]. Various meshing strategies were used for the remaining air region over the course of this project. In Paper I, a polyhedral mesh was chosen, which resulted in a high cell count to achieve the desired refinements. In Paper II, a hexahedral mesh was chosen, as it allowed for a better control of the refinement regions. Finally, for Paper IV, the software had implemented a better control

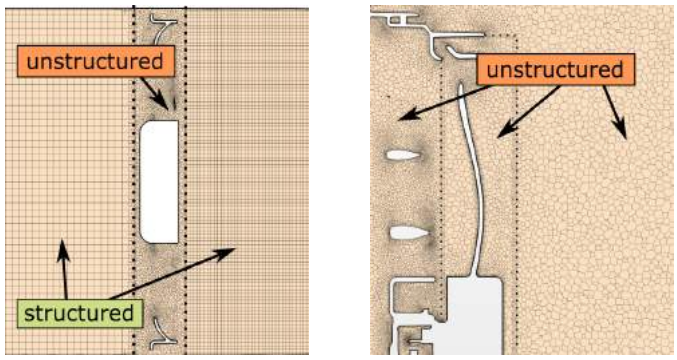

Figure 2.1: *Examples for the combination of different mesh types.*

mechanism for the polyhedral mesher as well, hence all meshes apart from the heat exchangers were polyhedral. This approach is preferable, since the internal flow is complex and polyhedral meshes are able to better resolve gradients due to their large amount of faces for each cell. It is therefore also the recommended mesh type for internal flow and heat transfer analyses [32]. Furthermore, it can lead to a higher conformity of the interfaces between the fan and the surrounding region. Figure 2.1 illustrates the two different meshing approaches.

The quality of the meshes was assessed by two different ways. The first was to start from a coarse mesh and successively refine the mesh in critical areas and monitor important properties and how they were affected by the increased mesh density. In Paper I and II, this was done for the air mass flow through the fan region and the pressure rise from the fan regions inlet to the outlet interface. The mesh was then refined until the change in the respective property is judged to be small enough not to give any further improvement. In Paper IV, only one mesh was used that has been based on previously employed mesh settings. The quality of this mesh was assessed by evaluating the ratio of resolved to modelled turbulent kinetic energy, as well as the normalised two-point correlation factor with respect to three reference points. According to Pope [44], at least 80 % of the total turbulent kinetic energy needs to be resolved for a valid LES. The two-point correlation was presented by Davidson [45] as a more reliable method, as it evaluates the amount of cells that is used to resolve a coherent structure. The normalised correlation factor of a flow variable between two points is defined as:

$$C^{norm}_{u_i' u_i'}(x_1, x_2) = \frac{\overline{u_i'(x_1) u_i'(x_2)}}{u^2_{i,RMS}(x_1)} \tag{2.2}$$

$C^{norm}_{u_i' u_i'}$ needs to be above a chosen threshold value for a minimum of 8 cells, preferably more, in order to resolve the large turbulent scales [45]. The results of this mesh quality assessment will be described in Chapter 4.3.

In order to resolve the boundary layer in the near-wall regions, prism layers are applied in combination with wall functions. The latter are used in turbulent flow simulations to account for viscous effects close to the wall, while keeping the cell count in the boundary layer low. Low-, high- and all-y^+ wall two-layer models are available, where y^+ is the non-dimensional wall distance as a function of the friction velocity u_τ:

$$y^+ = \frac{y u_\tau}{\nu}. \tag{2.3}$$

For the low-y^+ wall treatment, a number of cells cover the viscous sublayer ($y^+ < 5$), with the first cell centre placed within $y^+ < 1$. However, appropriate wall functions are still applied to provide suitable boundary conditions [32]. In the high-y^+ wall treatment, the first cell is placed in the log-law region ($30 < y^+ < 300$) and both the velocity distribution and the viscous effects are modelled with a wall function. The all-y^+ two-layer wall treatment uses so-called blended wall functions that aim at representing all three inner layers, including the buffer layer ($5 < y^+ < 30$). Even though it is not encouraged to place the first cell height in the buffer layer, the software developer claims that it gives reasonable results for this case. In the performed studies, the all-y^+ two-layer wall treatment was utilised to keeping the first cell within $y^+ < 1$ around the fan blades. In the remaining domain, areas of high- and low-y^+ can be found, while avoiding to place the first cell in the buffer region.

2.1.4 Heat exchanger modelling

Heat exchangers are a crucial part of a vehicles thermal management system. In automotive installations, the crossflow heat exchanger type is commonly used. An example of such an heat exchanger core can be seen in Figure 2.2. In these, a hot fluid passes through a number of small channels (red arrows), that are connected by thin fins. Through thermal conduction, the heat passes from the hot coolant fluid on the metal fins, that are convectively cooled by the air coming through the vehicles front openings (blue arrows). If the ram air does not provide a sufficiently large air mass flow to evacuate the required amount of heat from the coolant, additional air flow is provided by an axial cooling fan. The cooling fan can be positioned up- or downstream of the heat exchanger.

As the metal fins are building a very fine structure, it is not feasible to mesh this part in CFD in detail. Instead, the heat exchanger is commonly modelled as a porous medium, which accounts for the momentum loss the incoming air flow experiences when passing though the cooling module. The data for the pressure drop over the heat exchanger is provided for a range of mass flow rates by the manufacturer.

With this information, a porous viscous (P_v) and porous inertia (P_i) resistance tensor can be computed for the Darcy-Forcheimer equation:

$$\boldsymbol{s} = -\left(P_v \mu + P_i \varrho |\boldsymbol{u}|\right) \cdot \boldsymbol{u} \tag{2.4}$$

Equation (2.4) describes a sink term for the momentum equations that creates a pressure gradient in the porous cell. This approach is the most common method for simulations of automotive heat exchangers and has, amongst others, been used by [46, 47, 48].

2.1.5 Fan modelling

The modelling of moving parts, such as automotive cooling fans, in CFD is often a complicated and expensive problem to solve. One-dimensional fan models have been used in the past, that utilised the data from the fan performance curve to apply the pressure rise over the fan as a momentum source [49]. The downsides are that this method is unable to capture 3 D effects, such as swirls, and that the fan curve for the exact set-up needs to be known in advance.

With an increase of computational power, three-dimensional fan models are more often found in recent publications. Three-dimensional approaches have the benefit of including the rotor geometry and therefore do not need input data from experiments. The two most common approaches are the Multiple Reference Frame (MRF) and the Rigid Body Motion (RBM) or Sliding Mesh approach. These will be described in the following.

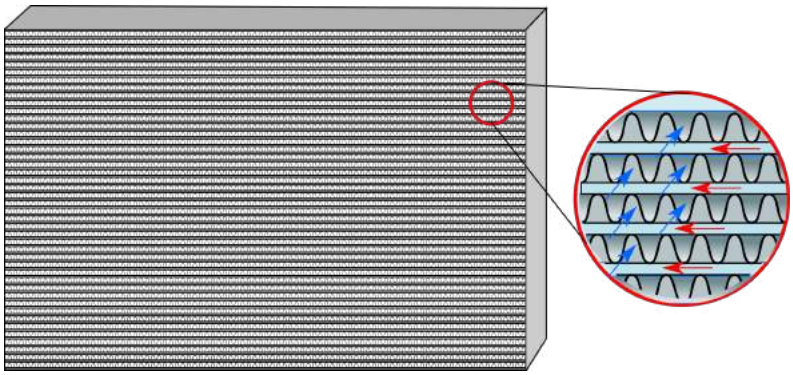

Figure 2.2: *Illustration of a crossflow heat exchanger.*

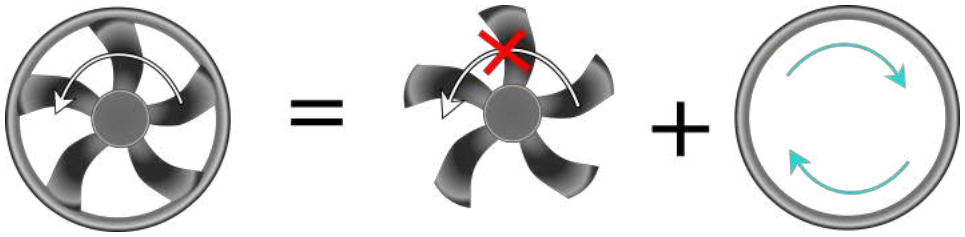

Figure 2.3: *Principle of the Multiple Reference Frame approach: the blade geometry is stationary, while the relative velocities are transformed into a rotating reference frame with the opposite sense of rotation.*

Multiple Reference Frame

The Multiple Reference Frame approach is a 3 D fan modelling technique that can be used for steady and unsteady simulations. In this method, the velocity vectors in a user-defined region around the fan blades are transformed into a rotating reference frame, using:

$$\boldsymbol{u}_{\mathrm{MRF}} = \boldsymbol{u} - \boldsymbol{\omega} \times \boldsymbol{r}, \tag{2.5}$$

where $\boldsymbol{u}$ is the velocity vector in the global (stationary) reference frame, $\boldsymbol{\omega}$ the rotational rate of the fan blades and $\boldsymbol{r}$ the radial position in the moving reference frame. By doing so, the air moves around the stationary blades in the same way the blades would rotate through the stationary air in reality. The approach is illustrated in Figure 2.3. All governing equations in the MRF region are then solved in the new reference frame and additional source terms for the centripetal and Coriolis acceleration are added to the RANS momentum equations [29].

This method has been very popular, since it requires less computational resources than the RBM approach and no prior knowledge over the fan curve. However, there are some challenges in correctly implementing it. All surfaces that are included in the MRF domain need to be rotationally symmetric with respect to the axis of rotation [28]. Given that the fan is usually hold in place by a number of spokes, this limits the extend of the domain in either up- or downstream direction. This can influence the performance of the MRF approach, as only axial and radial variations of the velocity field are allowed. If tangential dependencies were present, the flow conditions around one blade would differ from the rest of the fan and make the simulation results dependent on the rotor position. Multiple studies showed that a larger MRF region enables a more uniform flow at the interfaces and improves the prediction of the fan performance curve [29, 50, 51]. Kobayashi et al. [27] found that uneven flow over the interface can lead to an unphysical strain-rate which affects the flow behaviour at the interface. However, in automotive applications, the tight packaging in the underhood environment heavily restricts the lateral and radial dimensions of the MRF zone, and deviations are to be expected. In order to account

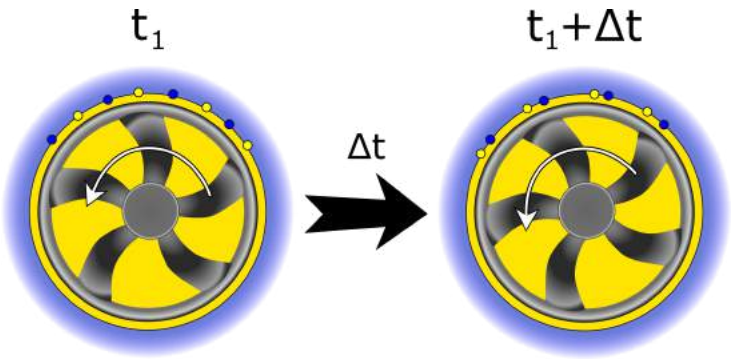

Figure 2.4: *Rotation of the fan region during one time step in the Rigid Body Motion (RBM) approach.*

for a possible effect of the blade position on the fan performance, Gullberg et al. [28, 52] showed promising results for averaging the flow field data for three different blade positions. The same approach is also evaluated in Chapter 3.1 of this thesis and referred to as the *Average MRF* method. In this approach multiple steady-state simulations are performed for different blade positions and the flow field data is averaged. As the blade position only changes slightly between the different steady-state runs, merely a small number of additional iterations are needed for the new position to achieve steady conditions and switch to the next rotor position.

In spite of the reported shortcomings of the MRF method, it is still often used due to its computational efficiency [49, 53, 54].

Rigid Body Motion

In the Rigid Body Motion (RBM) approach, sometimes also referred to as Sliding Mesh method, the user also defines a rotational symmetric region around the moving parts. This region is then rotated and the interfaces to the surrounding stationary region are re-computed in each time step (see Figure 2.4). Apart from being an inherent transient method, the rotation of a meshed region and updating the interfaces makes it considerably more expensive than the MRF method. Moreover, numerical inaccuracies can occur if flow structures are truncated over the interfaces in the process. Therefore, the mesh and time-step need to be chosen with care. A rotation by maximum one cell or roughly 1 deg per time-step is commonly recommended [32]. In some cases, larger time steps have been reported to have been successfully implemented [39] and should therefore also be investigated in order to reduce the computational costs.

If applied correctly, the resulting fan performance curve has been shown to be close to experimental data and the interaction between rotating and stationary parts

are well resolved. In contrast to the MRF approach, there are no requirements on the steadiness or rotational symmetry of the flow field. Hence, the location of the interfaces with respect to the blades are of lesser importance.

2.2 Experimental methods

The experimental part of this thesis was done by performing flow measurements with Laser Doppler Anemometry (LDA) or Laser-Doppler Velocimetry, as it is also referred to. This method uses the optical Doppler effect to measure the velocity of seeding particles in a flow [55]. The measurement principle and set-up is visualised in Figure 2.5.

A laser beam is split into two beams whereof one is phase-shifted by a Bragg cell. The two laser beams are then divided into beams of different wavelength, one wavelength per velocity component that is to be measured. The transmitter is focussing the beams in the measurement point, where the overlay of the two beams creates an interference pattern. When a particle passes through the measurement volume, it will diffuse the light of the laser beams in a frequency f_s that is proportional to the velocity of the particle:

$$f_s = u_i \frac{2 \sin \phi}{\lambda_0}, \tag{2.6}$$

where u_i is the velocity component perpendicular to the interference pattern, ϕ the angle between the two beams and λ_0 the incoming wavelength of the laser beams. Due to the phase-shifting of one of the beams, this interference pattern is moving, making it possible to detect the direction of motion of the particles. If the system is used in backscatter mode, the transmitter also acts as a receiver. The signal is then amplified by a photomultiplier and sent to a signal processor (Burst-Spectrum Analyser (BSA)) that is connected to a computer.

This technique was primarily chosen for this work due to its insensitivity to the thermal conditions and flow direction. When utilising conventional hot-wire anemometer and pressure probes, the flow direction in the measurement points needs to be known in advance in order to reduce the measurement error [21]. For isolated fans this is still feasible, but when including more upstream and downstream components in the experimental set-up, the flow becomes more chaotic and harder to predict. Moreover, LDA can measure reversed flow, does not require calibration and is classified as a non-intrusive measurement method [56]. However, it is sometimes debated that the necessary seeding particles present an intrusion into the flow. Also, as a small probe with a short focal length ($f = 50\,\mathrm{mm}$) was chosen for

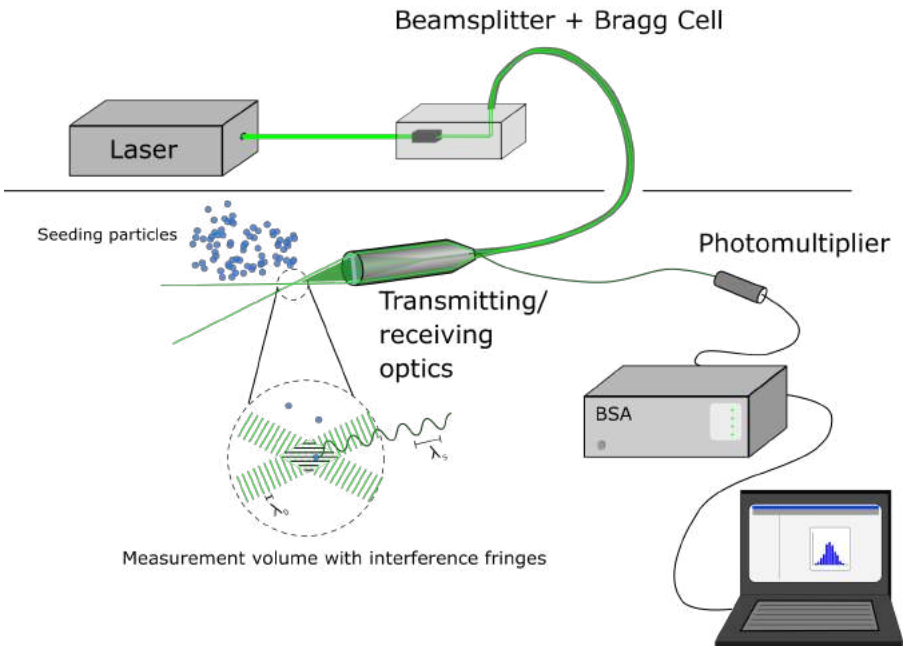

Figure 2.5: *Schematic illustration of the LDA principle and set-up.*

this study, the probe is positioned in the flow in close proximity to the measurement point and could therefore cause a small disturbance (see Section 2.2.1).

On the downside, LDA only provides point-measurements, which makes it time consuming when measuring a wake plane. Particle-Image Velocimetry (PIV) was considered as an alternative, given that it provides instantaneous information over a complete wake plane. However, PIV requires optical access to the measurement are from two perpendicular directions, which would be difficult to achieve in an actual underhood environment. When the LDA probe is operated in backscatter-mode, only one access is needed. Overall, LDA is a powerful measurement method for the purpose of this thesis and has been previously successfully applied in similar contexts [4, 5, 10, 16].

2.2.1 Influence of the probe geometry

The probe utilised for all measurements in this thesis is a two-component LDA probe with a focal length of $f = 50\,\text{mm}$, a diameter of $d = 14\,\text{mm}$ and a length of $l = 120\,\text{mm}$. Due to the short focal length, the probe has to be positioned in the flow. Therefore, it was important to ensure that the presence of the probe is not affecting the measured velocities.

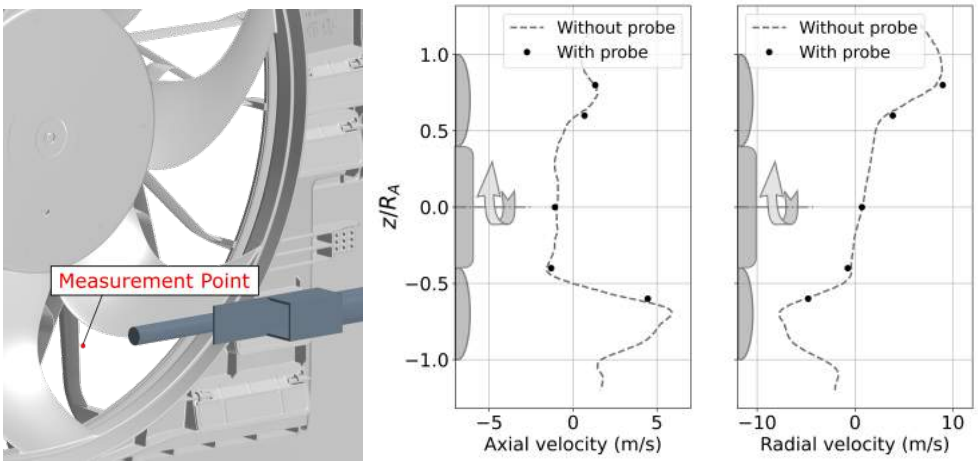

Figure 2.6: *Influence of the LDA probe on the velocity profiles in different measurement points along the vertical centreline*

As it was not possible to experimentally determine the true velocity without probe interference, it was chosen to perform CFD simulation with and without the probe geometry present in the flow. Even if the simulation results can deviate from the true velocity, the comparison between the two simulations can give an indication of the role the probe geometry has on the velocity in the measurement point. This assessment has been done for all experimental set-ups and is here exemplarily presented for the set-up from Paper IV. Six simulations were performed, whereof one reference case without the probe geometry and five with the probe being positioned at different locations along the vertical centreline. A comparison between the axial and radial velocity component with and without the probe representation shows good agreement for all positions (see Figure 2.6). It is therefore concluded that the presence of the probe only marginally influences the measurement results.

3 | Modelling of the axial cooling fan

This chapter deals with the different methods to simulate the effect of a rotating fan on the flow. In the first part, the different fan modelling approaches that were described in the previous chapter are validated against measurements downstream of an isolated fan. In the second part, a numerical study is presented on how inhomogeneities in the temperature and pressure field are transported through the MRF domain. The results presented here are a summary of Paper I and II.

3.1 Isothermal flow field prediction

3.1.1 Experimental set-up

The flow measurements were performed in Volvo Cars' Model-Scale Wind Tunnel (MWT), which is a closed-loop, slotted wall wind tunnel made for passenger cars in 1:5 scale. For the purpose of this study, a production fan was mounted centred in the test-section and the slotted walls were taped to facilitate the later comparison to CFD data (see Figure 3.1).

The fan and shroud utilised in this study can be seen in Figure 3.2. The test object is a so-called closed fan, where the blade tips are connected by a ring. It has eight forward swept blades and an outer diameter of $D = 0.38\,\mathrm{m}$. The rotation of the fan is anti-clockwise as seen from the downstream direction. The motor, positioned in the fan hub, is steered by a control unit which is mounted in the flow path downstream of the fan. The fan and motor are hold in place by four struts, which are also positioned downstream on the fan. The three bypass flaps in the shroud are taped closed to simplify the comparison to the numerical results.

Figure 3.3 provides a schematic overview of the experimental set-up in the test section from a birds eye perspective. The velocities were measured with a 2 D LDA

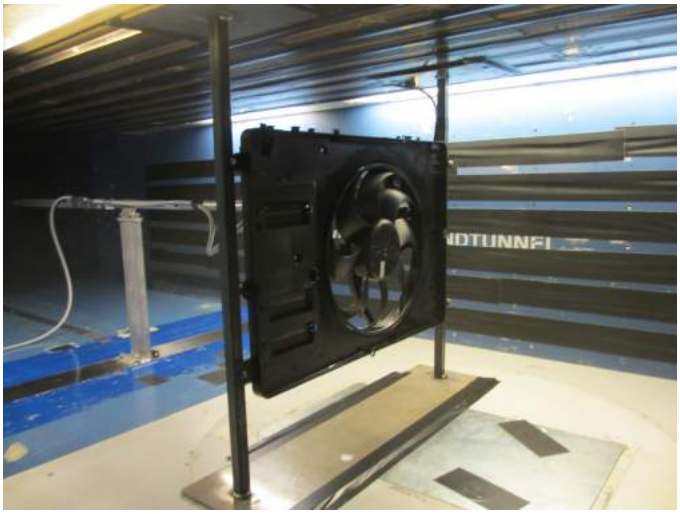

Figure 3.1: *Fan mounted in Volvo Cars' Model Wind Tunnel (MWT). The LDA probe is positioned downstream of the fan on a traverse.*

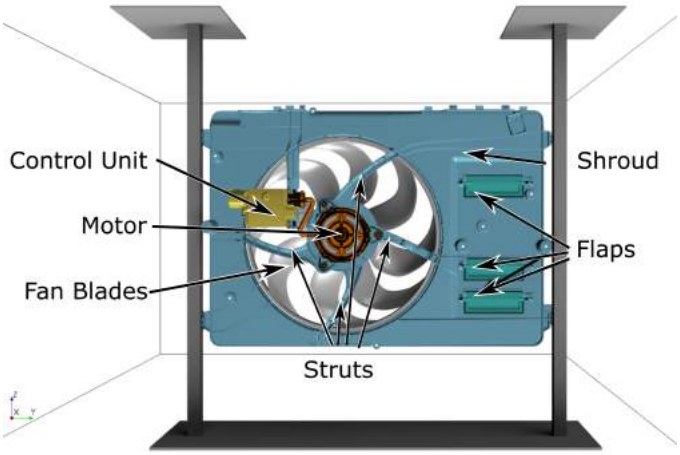

Figure 3.2: *Downstream view of the mounted fan and shroud.*

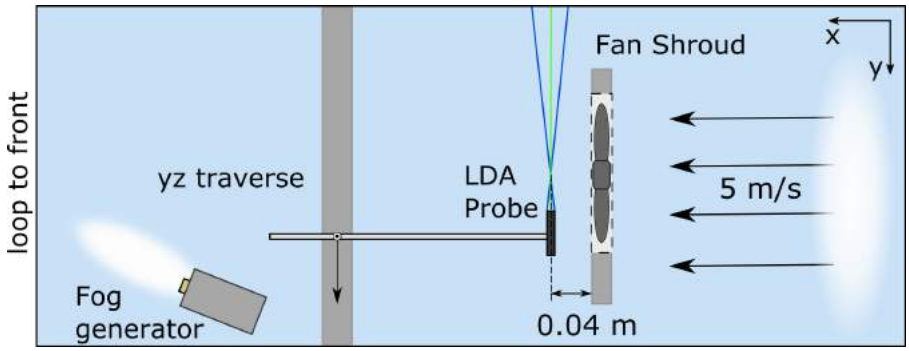

Figure 3.3: *Schematic overview over the experimental set-up in the test section.*

probe, mounted on a y-z traverse with the measurement plane 0.04 m downstream of the motor. The seeding was done with a fog generator placed downstream of the traverse, so that the fog had reached an even distribution when re-entering the test section. The seeding particles have an average size of $< 1\,\mu$m according to the manufacturer. The rotation of the fan was realised by using a pulse-width-modulator (PWM), and the rotational rate was controlled by using an optical tachometer. Thereby, the rotational speed could be set with an accuracy of ± 10 rpm.

The measurements were performed at a wind tunnel speed of 5 m/s and fan rotations of 1400 and 2800 rpm. These settings can be considered equivalent to a hill climb driving case, where the velocities through the cooling package are in this order of magnitude and the fan rotational rate can be anywhere between zero and full speed.

Figure 3.4 shows the measured areas of interest: the average velocity profiles were acquired in the vertical centreline, as well as along a vertical line with a 0.1 m lateral offset from the centre of rotation. The off-axis profile was of interest as the centre axis was covered to a large extend by the hub and struts, while the off-axis was mainly unobstructed and could therefore give additional information. Along these lines, measurements were taken in 5 mm increments. In addition, the complete wake plane was sampled in 20 mm increments in y- and z-direction. The measurements in each point were performed for 10 s or 10 000 samples, aiming for a minimum sample rate of 1 kHz. According to the manufacturer, this is suitable for acquiring time-averaged velocity data [55]. The accuracy of the measurements was determined by measuring the velocity profile downstream of the fan five times for 5 m/s at a rotational speed of 1400 rpm. It was found that the repeatability along the profile was within ± 0.3 m/s, while the statistical uncertainty for each measurement point was within ± 0.1 m/s at a level of confidence of 95 %.

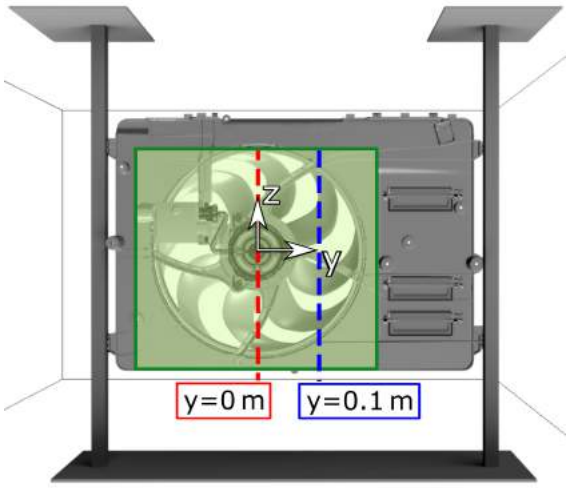

Figure 3.4: *Measurement areas downstream of the fan.*

3.1.2 Numerical set-up

Figure 3.5 shows the numerical representation of the physical set-up that was described in the previous section. It has the same cross-section as the test section in the MWT, but extends slightly further in x-direction to allow the flow to settle before reaching the outlet. The numerical set-up has a velocity inlet and pressure outlet boundary conditions up- and downstream, respectively. The surrounding walls are set up with a no-slip boundary condition. A polyhedral mesh is used both for the fan and the rest of the air domain, resulting in a mesh with a cell count of 13 million cells. The settings can be found in Appendix A.2.

The utilised fan models are the MRF, the average MRF (avgMRF) and the RBM model. For the avgMRF method, three different increments were investigated: 1 deg, 5 deg and 15 deg. As the fan geometry is symmetric with 8 blades, the fan position becomes identical every 45 deg, i. e. these increments result in 45, 9 and 3 different rotor positions, respectively. The simulations are carried out by using a RANS solver for the MRF and avgMRF model and a URANS solver for the RBM method. In all cases the Realisable k-ε two-layer turbulence model is used. The time-step in the unsteady simulations is set to $\Delta t = 5.5 \times 10^{-5}$ s at 2800 rpm and $\Delta t = 1.1 \times 10^{-4}$ s at 1400 rpm, which corresponds to a rotation of approximately 1 deg per time step and yielded a CFL number < 1 in the majority of the computational domain. After a transitional period of 5 fan rotations, the flow field was averaged for 10 additional revolutions to obtain the mean velocity field.

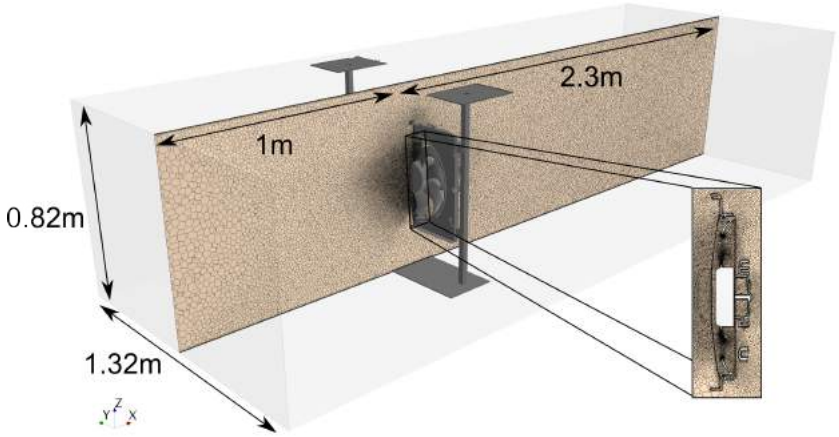

Figure 3.5: *Numerical set-up of the fan in the test section of the MWT.*

3.1.3 Results

The following section contains an overview of the results from the experimental and numerical set-up described above. The focus hereby lies on the maximum fan speed (2800 rpm), as the results for the lower fan speed followed a similar trend. Further results for the lower rotational rate can be found in [3] and [57].

Axial velocity distribution over a wake plane

Figure 3.6 shows the axial velocity field over the wake plane 0.04 m downstream of the fan for the MRF, average MRF and RBM approach and the experimentally obtained axial velocity field. The view is from the downstream direction. The hub, the struts and the control unit in the upper left quadrant can clearly be identified by the low velocity regions. Comparing the flow fields obtained by using the different simulation approaches, it is observed that the MRF method produces a more uneven flow field in between the struts, caused by the wake of the stationary rotor geometry. When using the average flow field over multiple blade positions (avgMRF), this imprint disappears and the flow field becomes more uniform, similar to the resulting flow field from the RBM method and the measurements. However, some differences remain: First, there are regions of elevated axial velocity to one side of the struts that only occur for the MRF based approaches (see area marked by red rectangle in Figure 3.6). With the RBM method, a more even flow distribution around the struts is observed. Another difference to the RBM and experimental data is that the velocity close to the control unit ($z/R \approx 0.75$) is considerably lower in both MRF based approaches. The same observations are made at a rotational rate of 1400 rpm.

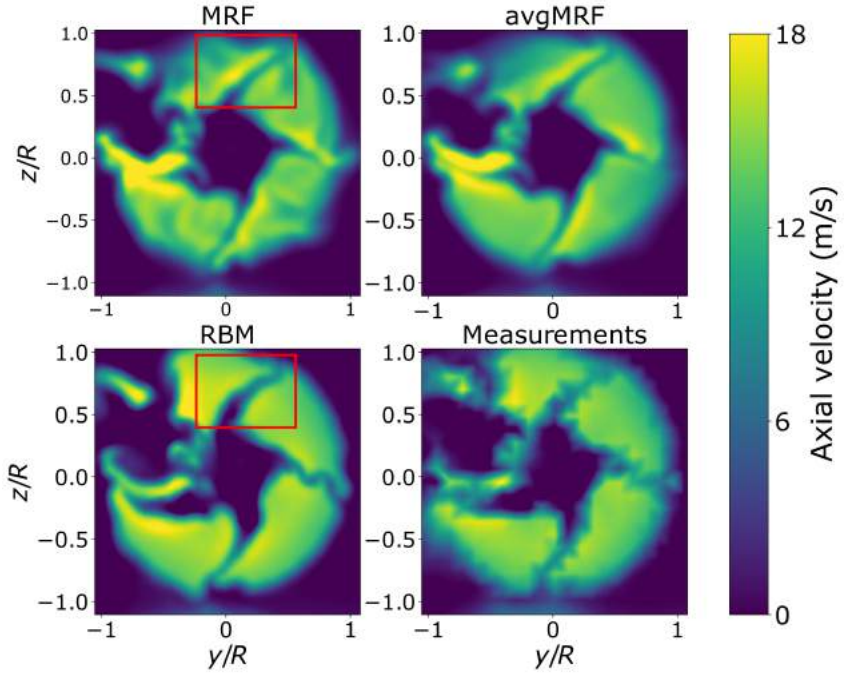

Figure 3.6: *Wake plane 0.04 m downstream of the hub, for the three simulation methods and the experimental results. The view is from the downstream direction, the fan rotation is anti-clockwise.*

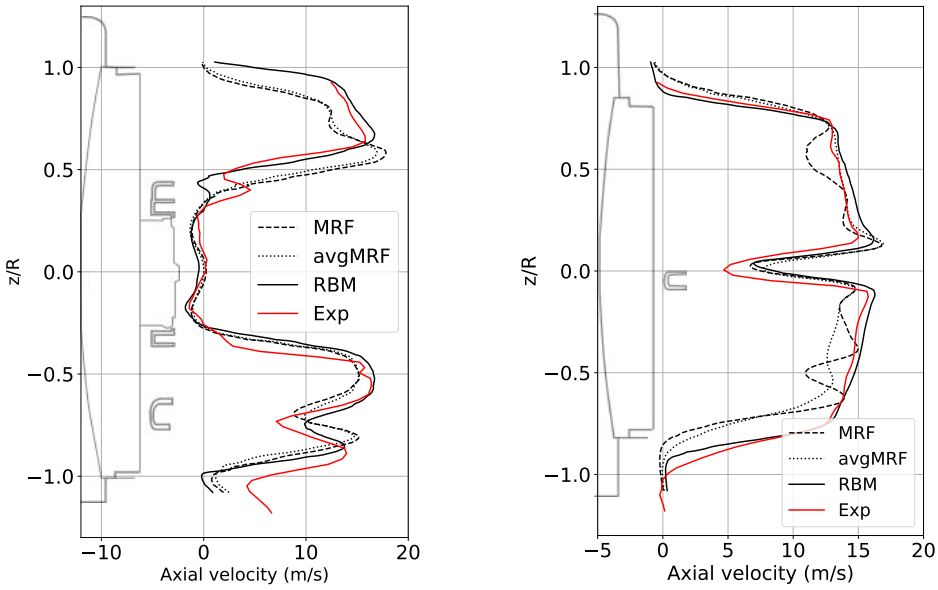

(a) $y = 0\,m$ **(b)** $y = 0.1\,m$

Figure 3.7: *Axial velocity profile 0.04 m downstream of the hub along two vertical lines, for the three simulation methods and the experimental results.*

Axial velocity profiles

For a better quantitative comparison, the profile of the axial velocity was measured with 5 mm increments along two vertical lines (see Figure 3.4). The results for 2800 rpm are shown in Figure 3.7 together with a respective cross-sectional view of the fan shroud and fan region. Along the centreline ($y = 0\,\mathrm{m}$), the axial velocity profiles predicted by the different approaches show relatively well agreement with each other and the measurements for the area downstream of the hub and the trend is captured in the lower half of the fan. The largest differences are found in the upper fan region, where the MRF based approaches exhibit considerably lower axial velocities. The RBM results follow the measured profile well, apart from a section just above the hub ($z/R \approx 0.4$). It is likely that these discrepancies were caused by small simplifications that were made to the CAE representation of the hub geometry, in order to improve the robustness of the simulations. Large fluctuations of the axial velocity occur for $y = 0.1\,\mathrm{m}$, when using the standard MRF approach. These fluctuations can be attributed to the wake of the single blades of the frozen rotor, since their influence disappears when averaging over multiple rotor positions. Figure 3.7b also shows that both the standard and the averaged MRF approach lead to a peak in axial velocity above the depicted strut ($z/R \approx 0.1$), which does not occur for the RBM approach or in the experiments.

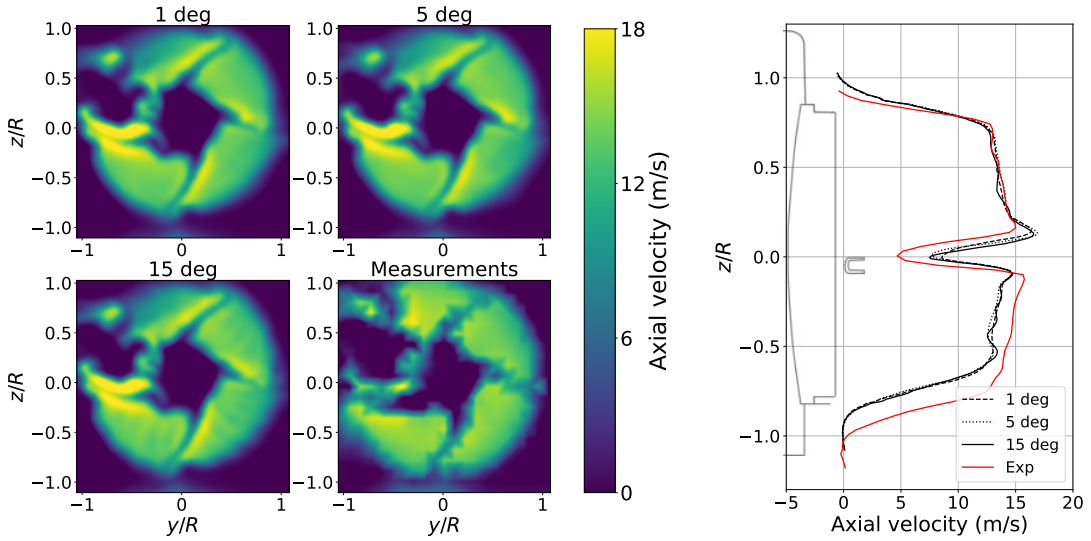

(a) *Wake plane (x=0.04 m)* **(b)** *Velocity profile at* $y = 0.1$ *m*

Figure 3.8: *Resulting axial velocity field for the avgMRF method performed with three different angle increments compared to the experimental results for a fan speed of 2800 rpm.*

Increments for the average MRF method

A prerequisite for the average MRF method is that the rotor geometry is rotational symmetric over the interval that is chosen. In the present study, the geometry repeated itself every 45 deg. The results for the averaged MRF method presented in the previous sections were obtained from averaging over 9 positions with a 5 deg increment. Additionally, a study was performed to investigate if the results could be improved by using a finer increment (45 x 1 deg) or if a coarser approach could be sufficient (3 x 15 deg). The results are presented in Figure 3.8. No notable difference between using a 1 deg and a 5 deg increment are observed. Both the results for the wake plane and the vertical lines look identical for those two cases. With the coarser increment of 15 deg, a slight influence from the blades wake can be noted in the wake plane. Along the centreline, the results are almost indistinguishable for all increments, and only small differences can be observed along the line for $y = 0.1$ m. In Figure 3.8b, the curve for the coarsest increment (3x15 deg) still inhibits small fluctuations, but they are negligible in comparison to the results from the standard MRF approach.

3.1.4 Summary

It could be shown that the frozen rotor position has a notable effect on the resulting flow field when using the MRF approach. These results could be notable improved by averaging the flow field over a relatively low amount of additional fan positions. However, the axial velocity around the struts and the control unit were not accurately captured. The RBM method showed close agreement to the measured axial velocities.

3.2 Transport of different field properties through the fan domain

Even though the previous section showed some deficiencies in using the MRF model, it is still a cost-efficient approach and hence widely used [49, 54]. To understand how other properties that are relevant for vehicle thermal management applications are affected by the switch in reference frame, a numerical study was performed on the same fan geometry with a local heat source upstream and different geometrical objects up- and downstream.

3.2.1 Numerical set-up

The computational domain is presented in Figure 3.9. The rotor geometry is the same that has been used in the previous study. It is placed in a cylindrical domain with a slightly larger diameter than the fan ($D_{\mathrm{cyl}} = 0.4\,\mathrm{m}$) which extends $2\,D$ upstream and $5\,D$ downstream of the fan region. A heat source is positioned $0.5\,D$ upstream of the fan, covering the lower half of the tube. The mesh is polyhedral in the fan region and hexahedral in the remaining air region, with different levels of refinement downstream of the fan (see Appendix A.2 for more details). The domain has a mass flow inlet and pressure outlet.

In the baseline configuration, the MRF region is tightly fitted around the rotor geometry. This results in a length of the MRF region of 60 mm. The rotational rate is set to 2800 rpm, which is the maximum speed for this fan. In the first part, it is investigated how different settings, such as the rotational speed and length of the MRF region, influence the temperature field downstream of the fan. In the second part, the settings for the MRF domain are kept constant to the baseline case, and different geometric objects are placed in proximity to the upstream and downstream interfaces of the MRF zone. This is done in order to study the effect that stationary structures, like struts or hoses, have on the flow field when using

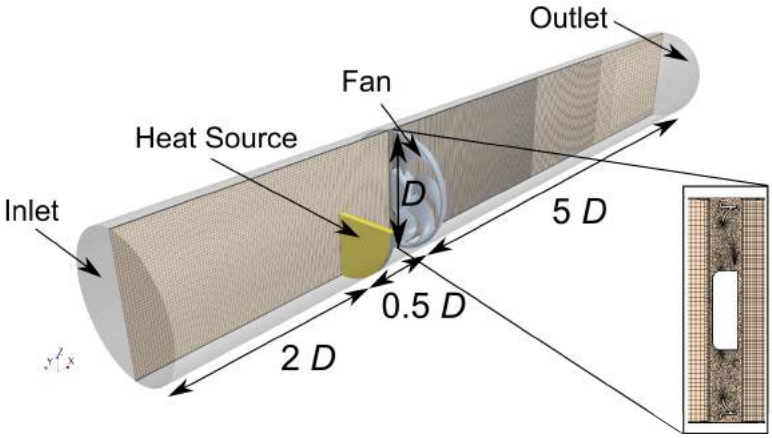

Figure 3.9: *Numerical set-up and domain*

the MRF approach. All simulations are performed once with and once without the rotor geometry in the MRF domain, in order to isolate the effect that comes from the transfer in reference frame and from the blades. Unsteady simulations using the RBM method served as a reference. The solver settings are identical to the ones described in Section 3.1.2, apart from the turbulence model, which was switched to an IDDES model with underlaying Spalart-Allmaras closure model.

3.2.2 Inhomogeneous temperature field

For this investigation, the temperature field changes between the upstream and downstream interface of the fan zone are studied. The results for the baseline case ($L_{\mathrm{MRF}} = 60\,\mathrm{mm}$, 2800 rpm) are shown in Figure 3.10, and compared the the corresponding results obtained with the RBM method.

From the results of the simulations using the MRF approach it can be noted that in the case (a) with blades , the temperature field experienced a rotation of approximately 90 deg, while in the case (b) without the fan blades, the degree of rotation is even larger ($\approx 140\,\mathrm{deg}$). With the RBM method, the temperature field remain unchanged between the up- and downstream interfaces when no blades are present (Figure 3.10d), which is to be expected. Due to interpolation errors over the interface, however, some diffusion occurs at the transition between the warmer and cooler flow region. When the blades are included (Figure 3.10b), no visible rotation of the temperature field is observed either. In general, small rotational effects could occur, dependent on the induced swirl by the fan [30]. In the cases that include the blades (a and b), an elevated temperature is observed at the circumference of the upstream interface, independent of the utilised fan model. This can be attributed to the flow around the fan ring, that transports higher temperatures from the down- to the upstream region.

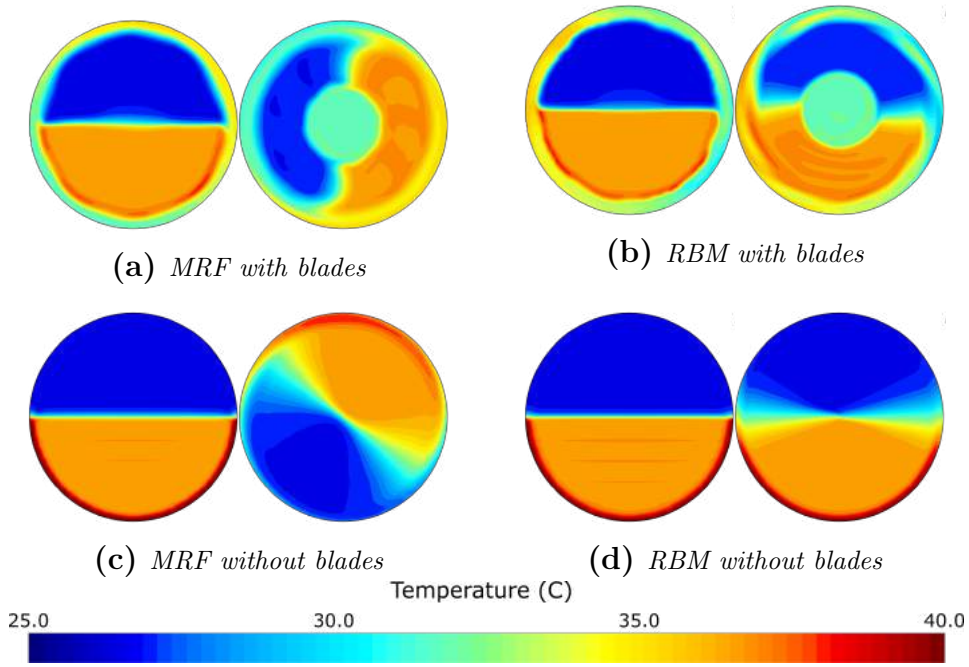

Figure 3.10: *Temperature field at the MRF upstream and downstream interfaces for the case with (a) and without blades (c) and the corresponding RBM results (b) and (d).*

The rotational effect that the temperature field experiences when using the MRF approach, can be explained as follows: Due to the frozen rotor position throughout the whole simulation, the streamlines of the absolute velocity (i. e. the streamlines in the global reference frame) often collide with the blades, which means that information would get lost. However, the streamlines of the relative velocity use the local reference frame, i. e. they are transformed into the rotating reference frame when entering the MRF region. Figure 3.11 shows the path of four streamlines of the relative velocity through the fan domain for the MRF (a) and the RBM (b) approach. The streamlines are coloured by temperature. The bottom two streamlines are passing through the heat source, and experience an increase in temperature, while the top two streamlines remain at ambient temperature up to the upstream interface. It can be seen that, when using the MRF approach, the top streamlines remain at the same temperature they had when entering the fan domain, while they change temperature according to the local conditions in the global reference frame when using the RBM approach. Hence, the rotation of the temperature field is inherent to the MRF approach.

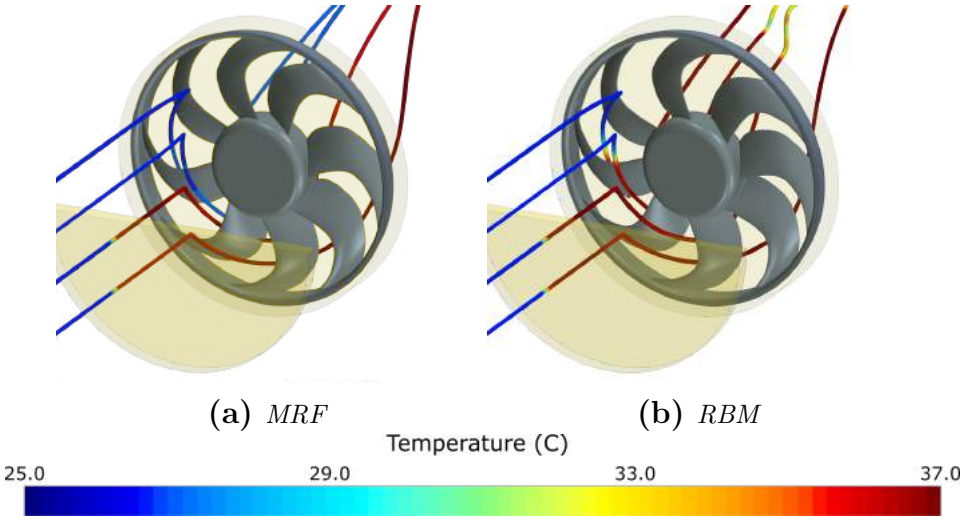

Figure 3.11: *Streamlines of the relative velocity coloured by temperature.*

In Paper III, it could be also shown, that the degree of rotation experienced by the temperature field, is dependent on the relation between axial and tangential velocity, as well as the length of the MRF domain. Riesterer [30] came to a similar conclusion and proposed a correction method based on the residence time of the fluid in the MRF region.

3.2.3 Disturbances to the flow field

As the temperature field is largely affected by the reference frame transformation in the fan region, it is also of interest to see to which extend the flow field is affected by this mechanism. For this study, three obstacles are introduced to the flow (see Figure 3.12). First, a cylinder is placed in close vicinity to the upstream MRF interface (case F1). Afterwards the same cylinder is positioned close to the downstream interface (case F2), and at last a cuboid, similar to the control unit from the previous study (see Figure 3.2), is placed downstream of the MRF region (case F3). All cases use a MRF domain with length $L_{\mathrm{MRF}} = 60\,\mathrm{mm}$ and the rotational rate is set to 2800 rpm. The upstream and downstream MRF interfaces are located at $x = -0.032\,\mathrm{m}$ and $x = 0.028\,\mathrm{m}$, respectively.

F1 – Upstream cylinder

Figure 3.13 shows the axial velocity distribution over the pipes cross-section from 0.05 m upstream to 0.05 m downstream of the fan blades (from left to right) for the case with and without blades run with the MRF approach.

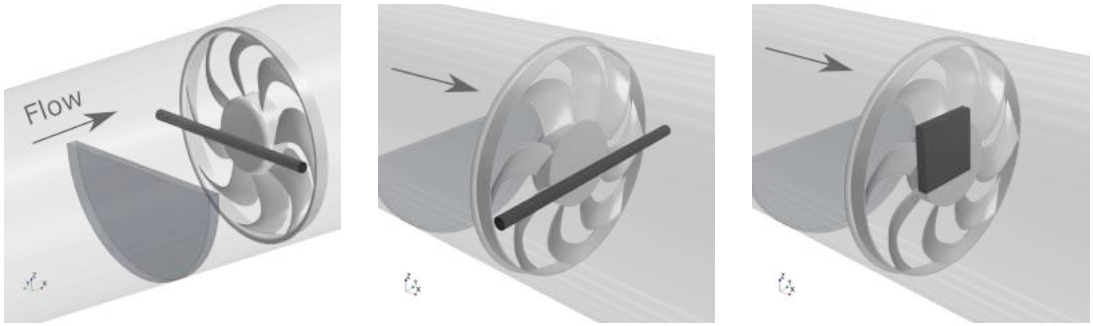

(a) *Case F1* (b) *Case F2* (c) *Case F3*

Figure 3.12: *Placement of different obstacles up- and downstream of the MRF interfaces.*

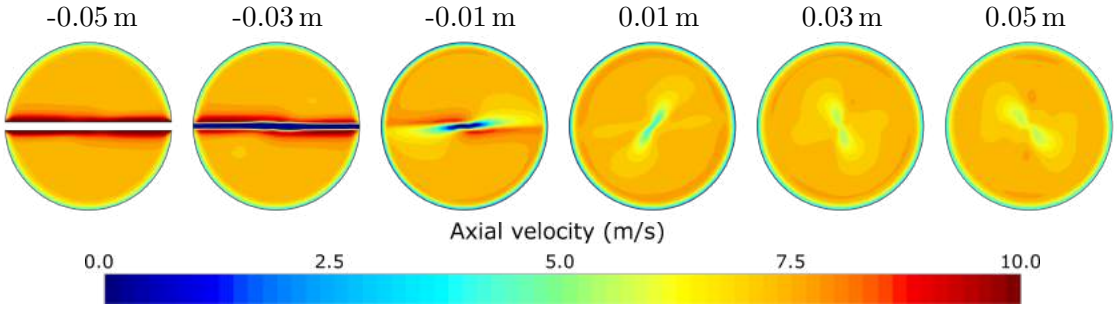

(a) *MRF region without rotor geometry.*

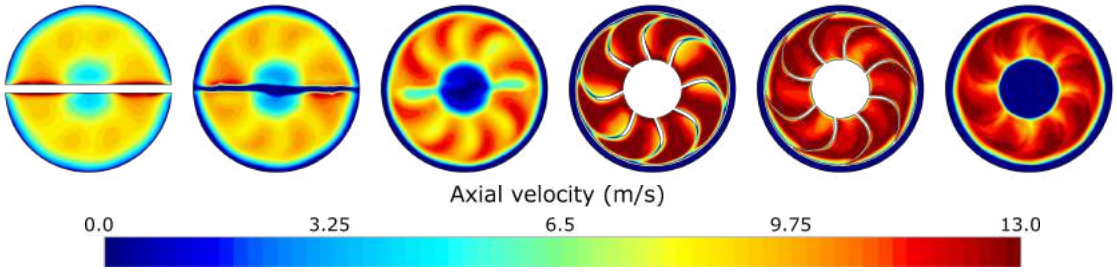

(b) *MRF region with rotor geometry.*

Figure 3.13: *Influence of a cylinder placed upstream of the MRF region on the axial velocity field from 0.05 m upstream (left) to 0.05 m downstream (right) of the blades.*

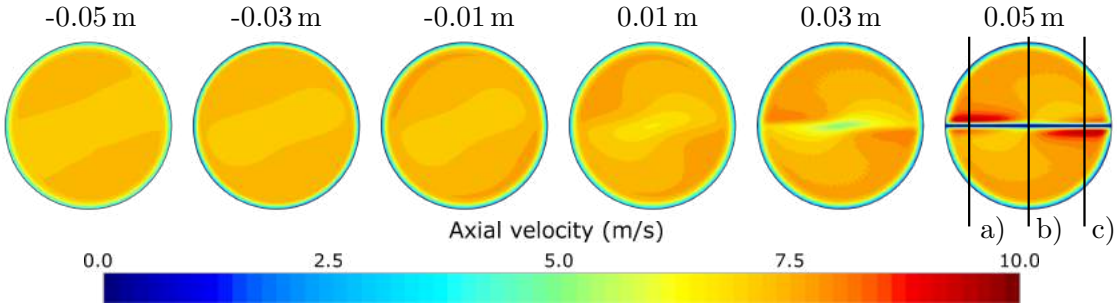

(a) *MRF region without rotor geometry.*

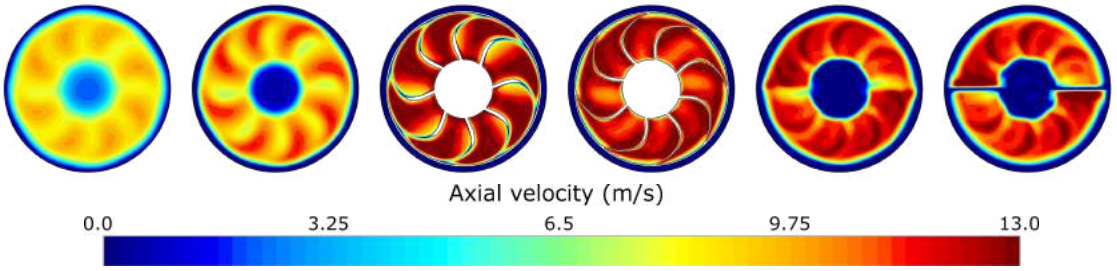

(b) *MRF zone including rotor geometry.*

Figure 3.14: *Influence of a cylinder placed downstream of the MRF region on the axial velocity field from 0.05 m upstream (left) to 0.05 m downstream (right) of the blades.*

In the case without fan blades, it is observed that the wake of the cylinder is rotated through the MRF domain, even though there has been no physical reason for this behaviour. The degree of rotation is the same as for the temperature field ($\approx 140\,\text{deg}$). When the fan blades are in place, the rotation of the wake can be followed until $x = 0.01\,\text{m}$. Then the effect from the blades superimpose the wake of the cylinder, and no trace is left downstream of the MRF domain ($x = 0.05\,\text{m}$).

F2 – Downstream cylinder

Placing the cylinder downstream of the MRF region resulted in a different behaviour than in case F1. As can be seen in Figure 3.14, a small effect on the axial velocity in the upstream region can be observed in the case without blades. This effect, however, is too small to be noted in the case with fan blades further upstream than $x = 0.03\,\text{m}$. The flow field appears to have undergone a slight rotation as well, which seems to take place between the cylinder and the downstream MRF interface.

In order to understand the origin of this effect, the distribution of the static pressure and its interaction with the flow field in the MRF region is plotted in Figure 3.15

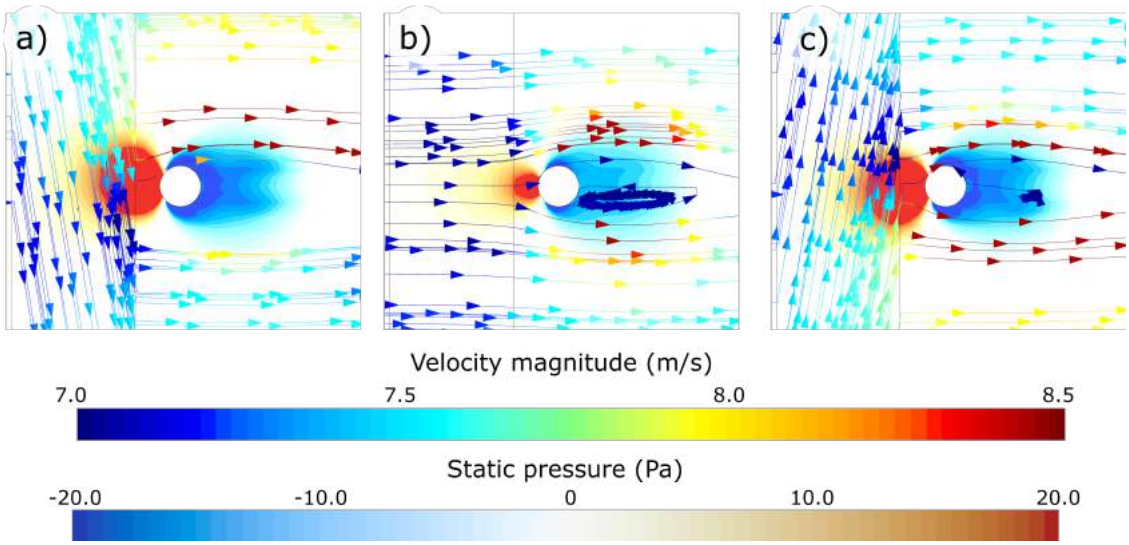

Figure 3.15: *Longitudinal view of the static pressure field and streamlines of the relative velocity coloured by magnitude, for case F2 (downstream cylinder) without fan blades. (a) left hand, (b) centre and (c) right hand plane (compare Figure 3.14).*

for the case without a rotor geometry in the MRF domain. It shows the static pressure field and the projected streamlines of the relative velocity on a plane for an x-z-cross-section for y =0.15, 0 and −0.15 m (marked a)-c) in Figure 3.14a). In areas where the pressure field that builds up in front of the cylinder reaches into the MRF domain, the streamlines in the fan region are notably decelerated. This means for case a), for example, that the absolute velocity of the streamlines exiting the MRF zone above the cylinder is significantly higher than the velocity of the streamlines that are passing through the high pressure zone first and are thereby decelerated. In the centre-plane ($y = 0$ m, b)), there is no rotation in the MRF domain, and the static pressure field also does not reach as far into the MRF domain as in location a). Therefore, the distribution is more uniform. In the third plane c), the flow in the MRF domain comes from below, which creates a lower velocity above the cylinder. These imbalances can also be observed in Figure 3.14a, first picture from the right and explains the uneven flow distribution around the struts in Figure 3.6. In the corresponding RBM simulation without blades, the pressure distribution around the cylinder would is identical for all three cut planes and similar in magnitude to plane b), where no additional rotational component is added to the velocity in the MRF region.

F3 – Downstream box

The last object investigated is a cuboid placed downstream of the MRF region. This object was chosen due to the effects of large objects on the flow field that were seen and described in Section 3.1.3 on the example of the control unit. Figure 3.16 shows

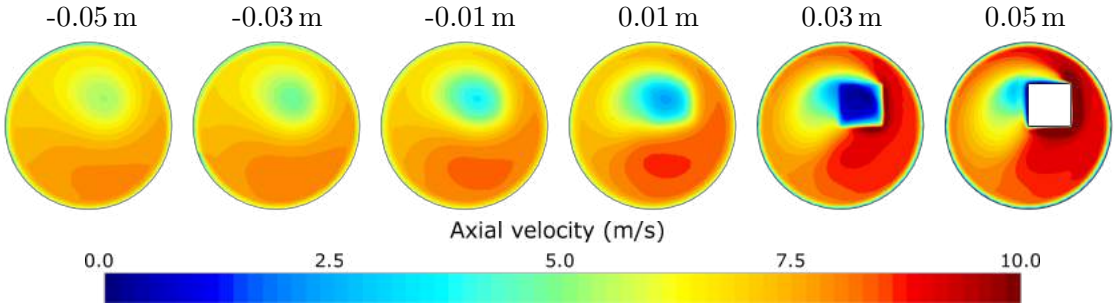

(a) *MRF region without rotor geometry.*

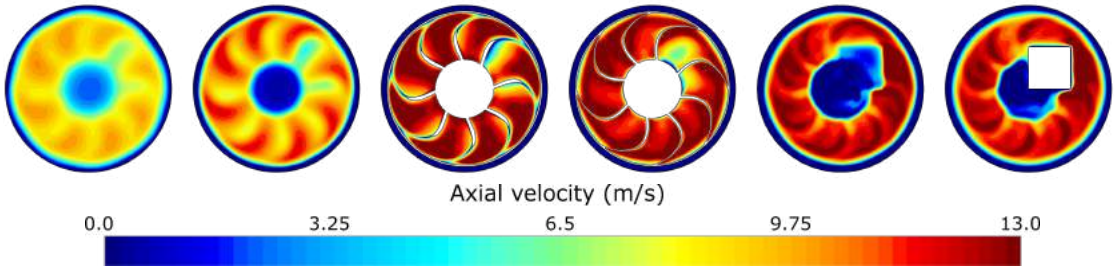

(b) *MRF zone including rotor geometry.*

Figure 3.16: *Influence of a cuboid placed downstream of the MRF region on the axial velocity field from 0.05 m upstream (left) to 0.05 m downstream (right) of the blades.*

the axial velocity field from 0.05 m upstream of the blades to 0.05 m downstream of them for the MRF simulation of the case without (upper row) and with (lower row) rotor geometry.

It can be seen that, even with the blade geometry in the fan zone, the cuboid has a notable influence on the flow field upstream of the MRF zone. In the case without blades, this can be observed as well, but a more notable effect is the imbalance in axial velocity that occurs close to the obstacle. When approaching the location of the cuboid, the velocities in the lower right half are considerably higher than in the upper left half. This can be explained by looking at the distribution of the static pressure around the cuboid and the projected streamlines of the relative velocity through the MRF domain (see Figure 3.17). Just as in case F2 (downstream cylinder) the pressure field propagates into the MRF domain and causes the streamlines there to decelerate. Given that the sense of rotation of the air in the MRF region is anti-clockwise (opposite of the clockwise rotation of the fan), the streamlines exiting the MRF zone before passing the high pressure zone, reach a considerably higher velocity than the streamlines that are decelerated due to the elevated pressure caused by the presence of the box and control unit, respectively.

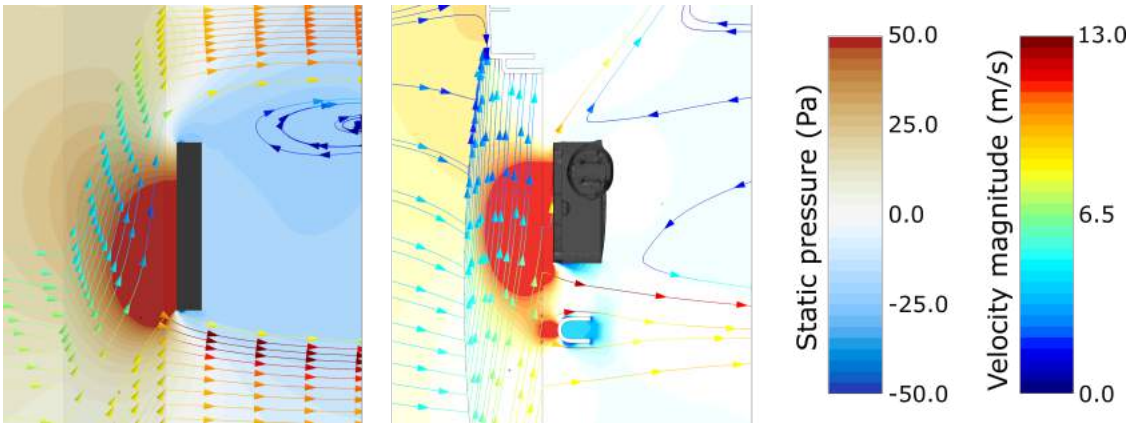

Figure 3.17: *Static pressure field and constrained streamlines of relative velocity for case F3 (left) and the control unit from Section3.1.3 (right), coloured by velocity magnitude.*

3.3 Summary

From the performed experimental and numerical studies, the following observations were made:

- The RBM approach yields the closest agreement to experimental data, but is also the most computational expensive method amongst the investigated fan models.
- The MRF method results in an uneven flow distribution in the downstream region, due to the frozen rotor position. This can be partially mitigated by using an average of at least three different rotor positions.
- Inhomogeneities in the temperature field are rotated by the switch in reference frame, when using the MRF approach. This is due to the fact that the flow information is transported with the relative streamlines through the different reference frame.
- Small flow disturbances in the upstream region would be similarly rotated, however, the effect from the frozen rotor position on the downstream flow field is larger.
- Any structure downstream of the MRF region can affect the flow distribution around it, if the static pressure build-up reaches into the MRF region, where it will decelerate the flow.

It is concluded, that the MRF method is computationally efficient. However, it is not suitable to use it in a narrow environment such as the underhood, that also included complex thermal processes.

4 | Underhood flow

In order to study the flow field in a vehicle-like installation, a simplified underhood environment was designed. This test rig was then used to investigate the effect of different front opening types and downstream blockages. The usage of a simplified rig allows for a good access with the measurement equipment and provides a more controlled environment than a production vehicle. First, the impact of different components on the flow field out of the fan was investigated experimentally. Then, a numerical study on some of the configurations was conducted and the results were validated against the measured data. The results presented here are a summary of Paper III and IV.

4.1 Simplified underhood environment

The simplified underhood environment is a cuboid test-stand that is build around an axial cooling fan, see Figure 4.1. It has the overall dimensions of 800 x 800 x 1000 mm (W x H x L), which is representative for a SUV-type vehicle. The width was set to the approximate space between the wheelhouses. The front design can be varied between a typical BEV and a HEV set-up. The BEV configuration only has an opening positioned in the centre of the lower half (630 x 150 mm (W x H)), while the HEV front also has an additional upper grille opening (700 x 240 mm (W x H)). The outlet spans over the complete lower third of the rear of the rig and has a height of 185 mm. Airguides connect the front openings to the cooling package, which consists of two radiator cores with the dimensions 654 x 556 x 26 mm (W x H x L), placed 10 mm apart, and a cooling fan. The heat exchangers serve as a flow resistance, but are not connected to a cooling circuit. In the test section, two different blockages can be installed. Both have the same overall dimensions of 570 x 570 x 400 mm (W x H x L), with the difference that one of the blockages has a sloped surface (45 deg) in the upper third in order to create an asymmetry. The boxes are placed on rails so that the lateral and longitudinal distance to the fan can be varied. Further details on the geometry of the testbed can be found in Appendix 6.

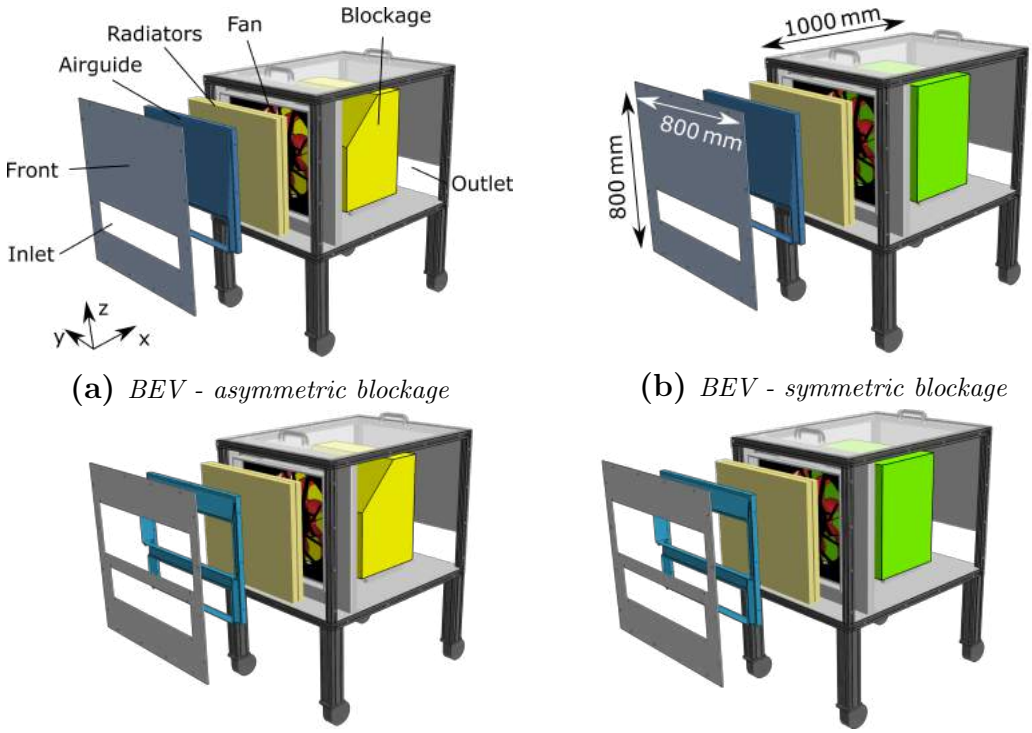

(a) *BEV - asymmetric blockage*

(b) *BEV - symmetric blockage*

(c) *HEV - asymmetric blockage*

(d) *HEV - symmetric blockage*

Figure 4.1: *Simplified underhood environment in the different configurations.*

4.2 Measurements

4.2.1 Set-up

The experimental set-up can be seen in Figure 4.2. The measurements were performed using a 2 D LDA probe. The rig has a slot opening on the side, through which a traverse arm was inserted. The traverse has two degrees of freedom and can move in z- and y-direction.

The fan used in this study has seven blades and a radius of $R = 0.25\,\mathrm{m}$. The measurements were performed for the fans maximum speed of 2400 rpm. The sense of rotation of the fan is clockwise as seen from the downstream direction. Additional measurements at 1200 rpm did not reveal any further information. The data was acquired along the horizontal and vertical centreline, as well as in a wake plane, for $x/R = 0.2$ downstream of the fan motor (see Figure 4.3). Due to the vertical position of the probe when measuring the y-component of the velocity vector, it was not possible to measure the lower third of the fan wake. However, little change is expected in this area, given that the main differences in the front openings and in the different blockages is located in the upper part of the rig.

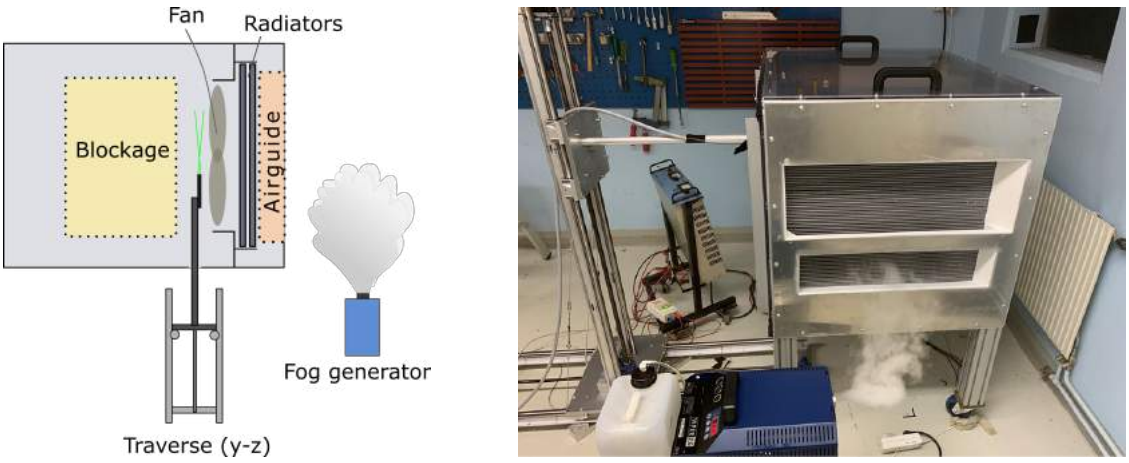

Figure 4.2: *Experimental set-up. Left: Schematic overview of the experimental set-up including the fog generator and the traverse (top view). Right: Photo of the actual setting.*

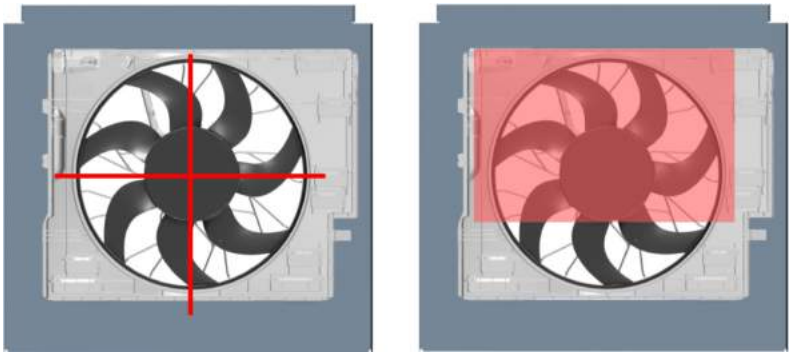

Figure 4.3: *Downstream view of the fan including the horizontal and vertical measurement lines (left) and wake plane (right) at* $x/R = 0.2$.

.

4.2.2 Uncertainties

The accuracy of the measurements was quantified using repeated measurements on different days on the vertical centreline of the fan for both front configurations. According to the "Measurement Good Practice Guide" by the National Physical Laboratory [58], between 4 to 10 measurements should be taken when assessing the standard deviation of an unknown quantity. Due to time limitations, five repetitions for each airguide configuration (BEV/HEV) without downstream blockage were performed. In the majority of measurement points the accuracy for the x- and z-component is lower than $\pm 0.25\,\mathrm{m/s}$ with single points in the shear-layer between the low-velocity hub region and the high velocity tip region reaching uncertainties between 0.5 and $1\,\mathrm{m/s}$. For the y-component the majority of measurement points are within an uncertainty of $\pm 0.4\,\mathrm{m/s}$ with single points in the tip region reaching uncertainties between $0.5\,\mathrm{m/s}$ and $1\,\mathrm{m/s}$. The slightly higher average uncertainty for the y-component is possibly due to the change of the probes orientation, which made it more difficult to seal the side opening through which the traversing pole enters the test section to the same degree as for the horizontal probe position. The statistical uncertainty of each of the three velocity components in each measurement point was found to be less than $\Delta u_i = \pm 0.1\,\mathrm{m/s}$ at a level of confidence of 95 %.

By modifying the orientation of the probe, all three components of the velocity vector can be obtained through successive measurements in the same points (see Figure 4.4). As the x-component is captured for both probe orientations, a comparison was performed on the centreline to ensure that the switch in probe orientation has no effect on the velocities in the measurement point. The test was performed at a fan speed of 2400 rpm for both front configurations with an empty test section. From the velocity profiles in Figure 4.5, it can be seen that the velocity profiles are following the same trend, independent of the probes orientation. The difference in

Figure 4.4: *Positioning of the 2D LDA probe in the test section. Left: x- and z-component, right: x- and y-component of the velocity vector are measured.*

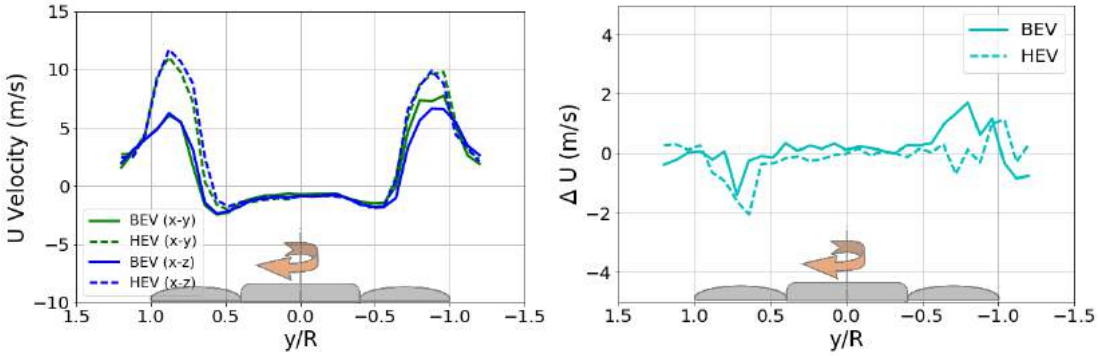

Figure 4.5: *Left: Horizontal axial velocity profile for an empty test section with the BEV and HEV front respectively, for both probe orientations. Right: Absolute difference in axial velocity.*

absolute axial velocity is, for the majority of points, within the margin of measurement uncertainty apart from the tip regions where slightly larger differences can be observed.

4.2.3 Results

The results are presented in three stages. First, only the influence of the front openings is of interest, and therefore the test section is empty. In a second stage, the effect of the blockage types on the flow field downstream of the fan is studied for both front configurations. Lastly, the relative position between the two blockages and the fan was investigated to understand its effect on the flow topology.

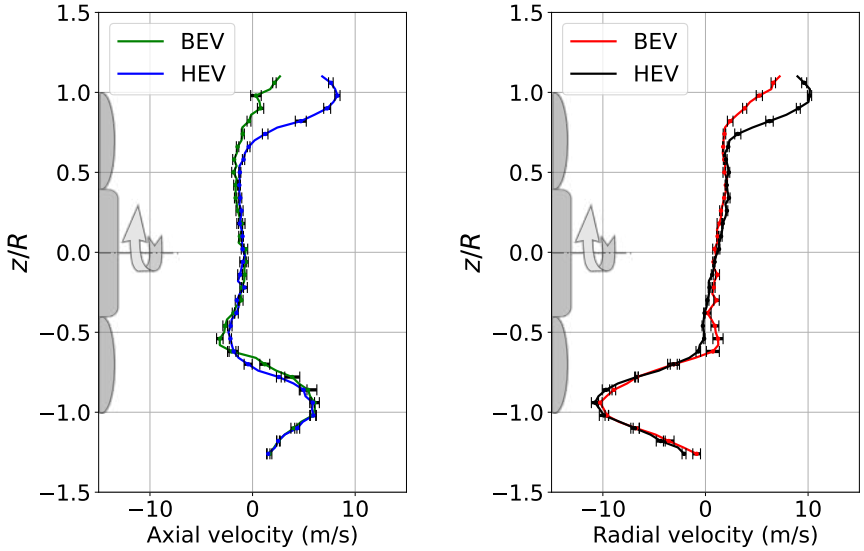

Figure 4.6: *Axial and radial velocity profiles along the centreline at $x/R = 0.2$ downstream of the fan for the BEV and HEV airguide configurations without blockage.*

Influence of the front openings

In order to isolate the effect that the different front openings have on the flow field downstream of the fan, a comparative study was performed on the test rig with an empty test section. This set-up also serves as the reference to which later configurations are compared to. Figure 4.6 shows the axial and radial velocity profiles in the vertical centreline for both configurations. The black markers indicate the measurement accuracy obtained from repeated measurements along the vertical centreline. In the lower and central part of the wake, the velocity profiles show close to no differences between the BEV and the HEV configurations. In the upper tip region, however, the absence of the upper grille opening can clearly be noted for the BEV configuration, with the axial velocity component being 5-8 m/s, and the radial velocity component approximately 3-5 m/s lower than in the HEV set-up.

In Figure 4.7a, the wake plane at $x/R = 0.2$ is coloured by velocity magnitude and the vector field shows the flow behaviour in this plane. The view is from the test section towards the fan. The hub and outer diameter of the fan are indicated by dashed lines and the direction of rotation by an arrow pointing in clockwise direction. As was previously observed, the velocity magnitude in the BEV configurations is notably reduced in the upper area. The low-velocity region in the hub area, is of similar shape in both configurations.

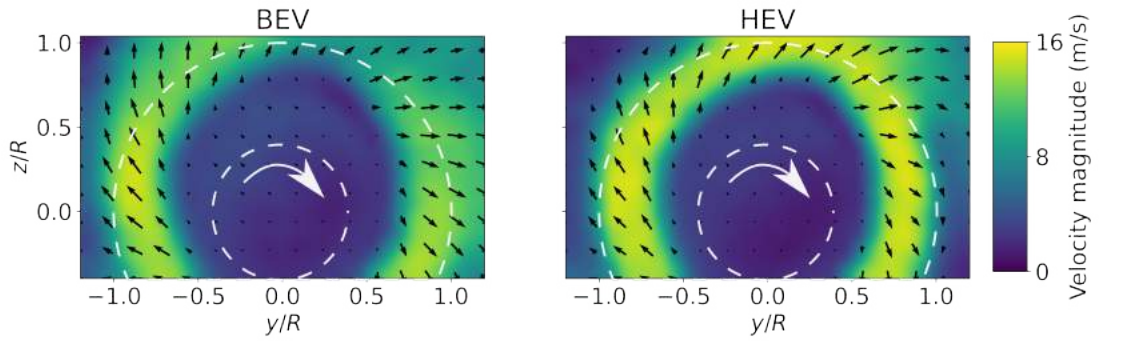

(a) *Velocity field*

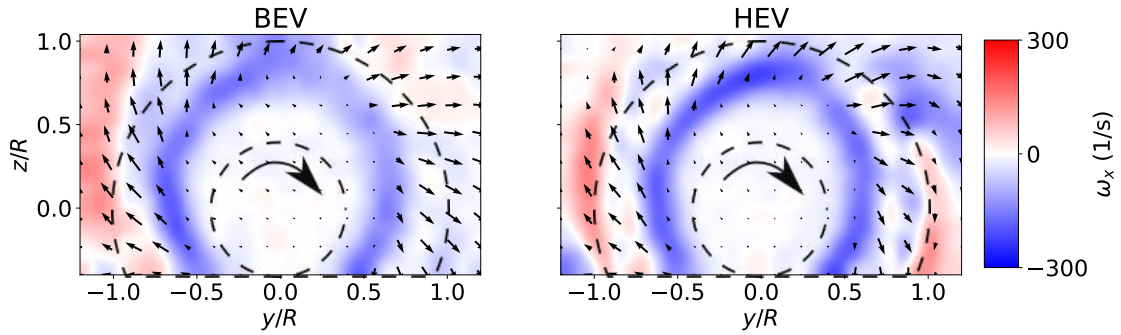

(b) *Vorticity around the x-axis*

Figure 4.7: *Wake plane at $x/R = 0.2$ for the BEV and HEV airguide for the reference configuration.*

Figure 4.7b shows the x-component of the vorticity vector, which was obtained by calculating the gradients of the velocity field from the measured data:

$$\omega_x = \frac{\partial w}{\partial y} - \frac{\partial v}{\partial z} \tag{4.1}$$

where v and w are the y and z-components of velocity vector, respectively. In the chosen coordinate system, the positive sense of rotation for the vorticity around the x-axis is anti-clockwise, hence it is opposed to the rotation of the fan. This results in a larger negative vorticity region around midspan of the fan for both configurations. The difference in velocity magnitude in the upper fan region also yields in a lower x-vorticity for the BEV set-up than in the HEV configuration. The vorticity field for the HEV front openings exhibit a generally more symmetric behaviour outside of the fan region. Two regions of positive vorticity are noted at around the three and nine o'clock positions, extending in clockwise direction. In the BEV configuration a large area of positive vorticity can be seen on the left hand side, outside of the fan region. These regions originate from the interaction between the fan wake and the walls. On the right-hand side of the fan, however, the vorticity is close to zero and the sense of rotation opposes the one that was observed for the HEV configuration.

Effect of downstream blockages

In the next step, two different blockages were introduced to the test section and measurements were performed for each of them with both front opening configurations. The results are compared to the reference case without any objects in the test section.

Figure 4.8 shows the velocity vectors in the vertical centreline at $x/R = 0.2$ for (a) the reference case, (b) including the symmetric and (c) the asymmetric obstruction. First, it can be seen that the axial velocity component in the tip region increases by introducing a downstream obstacle. This is observed for both inlet configurations and possibly caused by the blockages restricting the cross-section of the testbed and thereby accelerating the flow around it. In addition, the boxes also suppress a recirculation in the test section, which could have contributed to the strong radial flow in the reference cases. The second point of interest is the flow behaviour in the hub region. The small, but noticeable, reversed flow in the hub region of the reference case is reduced to practically zero when introducing a symmetric blockage. In the set-up with the asymmetric blockage, the sloped front causes a recirculation, which leads to an increased reversed flow in the hub area. This is especially visible in the BEV configuration, due to the reduced air flow in the upper part of the fan, which gives the recirculation zone more room to develop.

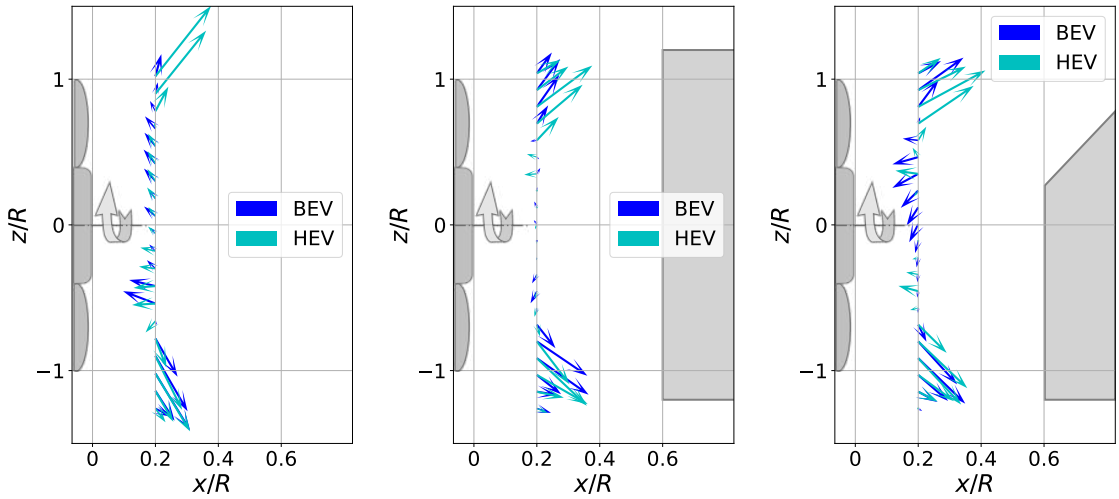

(a) *Reference (no blockage)* **(b)** *Symmetric blockage* **(c)** *Asymmetric blockage*

Figure 4.8: *Qualitative display of the velocity vectors in the centreline ($y/R = 0$) with different blockages at $x/R = 0.6$.*

The measured wake planes at $x/R = 0.2$ downstream of the fan are shown in Figure 4.9 for the symmetric and asymmetric blockage. In the case with a symmetric obstruction, the velocity magnitude in the hub region has notably increased for both inlet types in comparison to the reference case. As it was shown in Figure 4.8b that the axial and radial velocity components are close to zero in that area, this increase can be attributed to a gain in tangential velocity. This is also confirmed when looking at the vector field in Figure 4.9a, which forms a distinct swirl in the y-z-plane for both airguide configurations. For the BEV set-up, the centre of rotation can be identified by a small low-velocity region at the upper edge of the hub ($y/R \approx 0$, $z/R \approx 0.4$). In the HEV configuration, the low-velocity region is slightly larger and located closer to the centre of rotation of the fan. The difference can be explained by the higher air mass flow in the HEV case, due to the upper grille opening, which keeps the flow more centred. In the set-ups with the asymmetric blockage (Figure 4.9b), a low-velocity region occurs in the hub region for both airguides, which is similar to the reference case. In the BEV case, a downwash occurs, which is neither found in the HEV set-up nor the configuration without a blockage, which is a result of the recirculation along the sloped surface. For both airguide types, the wake appears to have shifted in negative y-direction. The reason for this behaviour could not be determined from the measurement data.

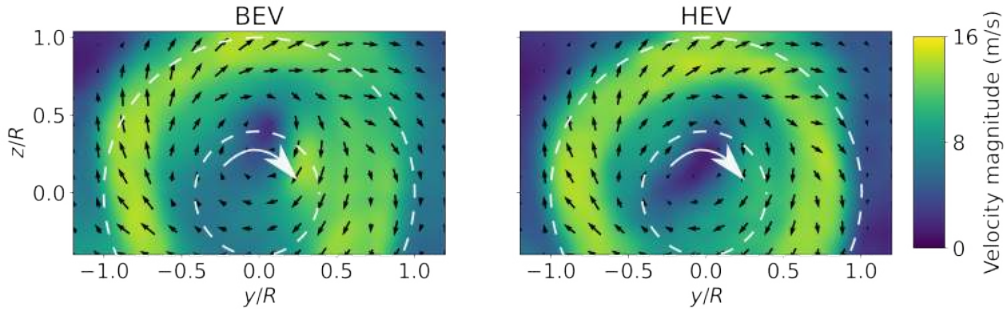

(a) *Symmetric blockage*

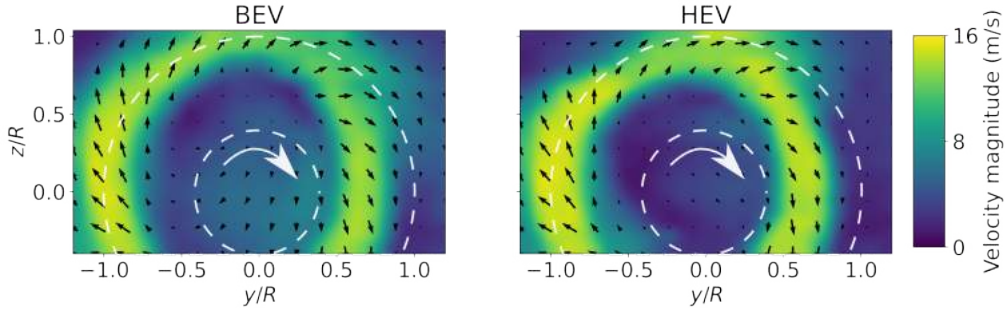

(b) *Asymmetric blockage*

Figure 4.9: *Wake plane at $x/R = 0.2$ with different blockages installed for the BEV and HEV airguides coloured by velocity magnitude.*

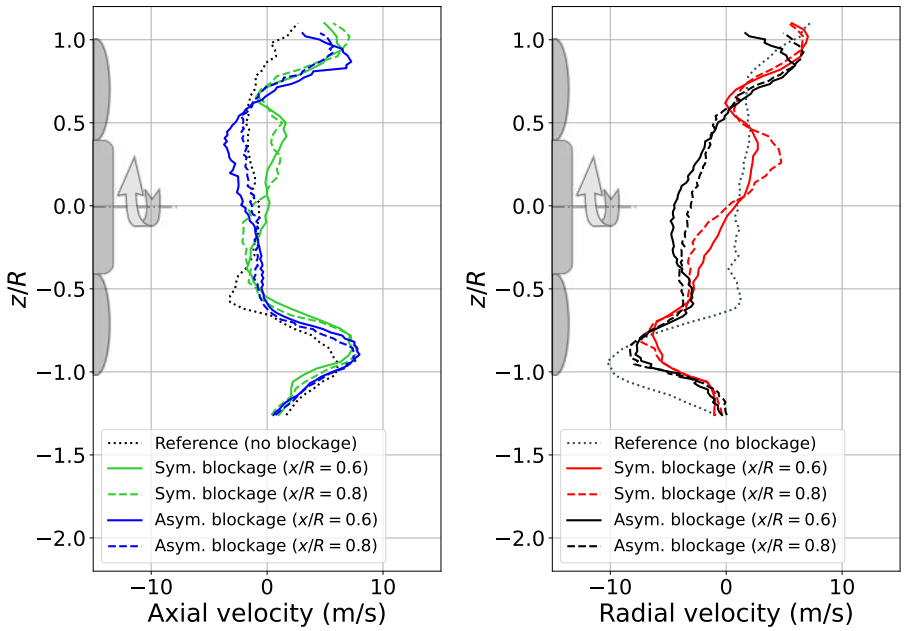

Figure 4.10: *Velocity profiles along the vertical centreline at $x/R = 0.2$ downstream of the fan for different blockages and their longitudinal positions with respect to the fan in the BEV configuration.*

Relative placement of blockages to fan

The position of the two blockages was first varied in longitudinal (x) and then in lateral (y) direction for the closest x-position to the fan ($x/R = 0.2$). For the investigated longitudinal distances, close to no effect on the axial velocity profiles was observed, independent of the airguide configuration and blockage type. This is exemplarily shown for the BEV configuration in Figure 4.10 and agrees with the findings of Khaled et al. [10]. The radial velocity profiles show some changes in the hub region, especially for the set-ups that included a symmetric blockage. As it was seen in the previous section that the symmetric blockage notably restricts the development of the flow in the downstream region, moving the blockage further away from the fan allows the flow to expand in radial direction.

The variation of the lateral position has no effect on the velocity profiles in the BEV configuration, independent of the blockage type. For the HEV configuration, a small influence on the axial and radial velocity profile is found in the hub region of the set-ups that included the symmetric blockage. The velocity profiles in the HEV installation with the asymmetric blockage were less affected by the variation of the lateral position of the blockage.

4.3 Simulations

In the final step of the project, the simplified underhood environment is recreated in CFD to assess the ability of state of the art simulation methods to capture generic underhood flow behaviour.

4.3.1 Numerical set-up

For the simulations, the geometric representation of the rig is inserted in a computational domain with the overall dimensions representative of the room in which the measurements were performed. Figure 4.11 shows how the complexity of the set-up is gradually increased from only a fan in the test section without any components installed up- or downsteam (Stage I), to including the radiator cores and the two frontend designs representing a BEV and HEV inlet (Stage II), to finally adding to Stage II a symmetric blockage 0.15 m downstream of the fan motor (Stage III).

Two different fan geometries are studied, referred to as Fan A and B. Fan A has been used in the experimental investigation of installation effects in the simplified underhood geometry in the previous section and is representative of the cooling fan of a larger SUV. Fan B is an axial cooling fan from a C-segment vehicle and was part of the study in Chapter 3. Figure 4.12 shows the installed fans from an upstream and downstream perspective. There are a number of differences in the fan design: Fan A has a larger diameter than Fan B, and 7 instead of 8 blades. Furthermore, the struts that hold the fan motor in place are positioned upstream of the rotor for Fan A and downstream for Fan B. The maximum rotational speed is 2400 rpm (Fan A) and 2800 rpm (Fan B), respectively. The fans are mounted centrally in the test section with identical locations of the fan axis, but different sense of rotation. Seen from the downstream direction, the sense of rotation for

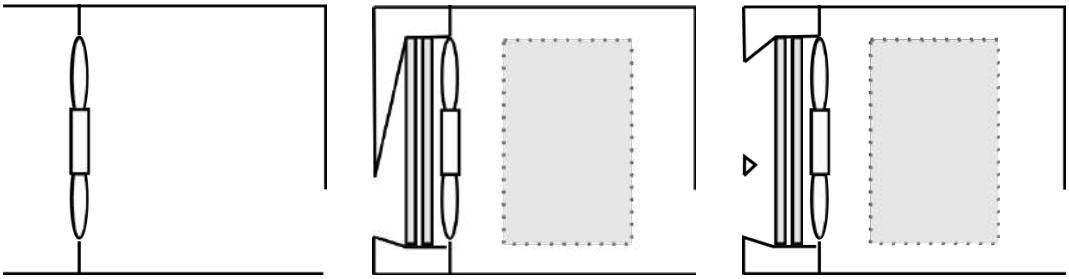

(a) *Stage I - only Fan* **(b)** *Stage II+III - BEV* **(c)** *Stage II+III - HEV*

Figure 4.11: *The three stages of complexity in the set-up. Stage II is without and Stage III is with the downstream blockage.*

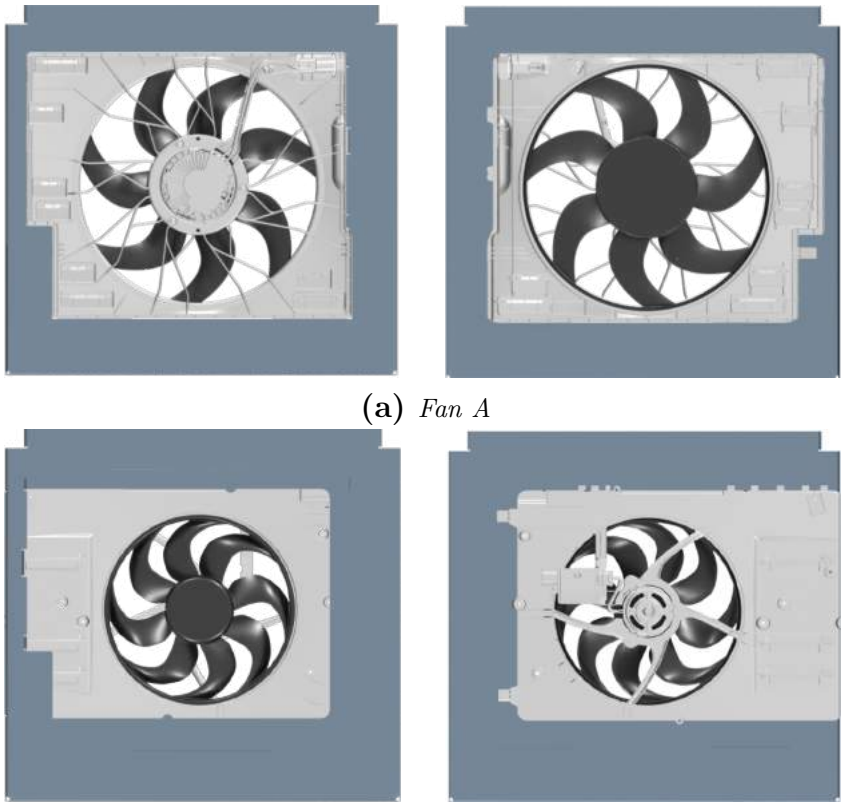

(a) *Fan A*

(b) *Fan B*

Figure 4.12: *View of the two fans from the upstream (left) and downstream (right) direction.*

Fan A is clockwise and for Fan B anti-clockwise. Additional information on the two fans can be found in Appendix A.1.

The mesh consisted of polyhedral cells with different levels of refinement, that can be seen in Figure 4.13 for Fan A in the BEV configuration without downstream blockage. The mesh settings can be found in Section A.2. A low y^+ approach is applied for the airguides and fan blades and a high y^+ for the remaining surfaces.

The quality of the mesh is evaluated using the DDES blending factor and the ratio of resolved turbulent kinetic energy in the centre-plane. Furthermore, the normalised two-point correlation coefficient (see Equation (2.1.3)) was calculated with respect to three reference points in the measurement plane (see Figure 4.14a). Figure 4.14b shows the variation of $C_{u'u'}^{norm}$ with increasing distance in x-direction. It can be seen that the minimum requirement of 8 correlated cells, stated by Davidson [45], is exceeded for all three reference points. The curves for the respective velocity components in and along the y- and z-direction are not presented here, but show equally good correlation.

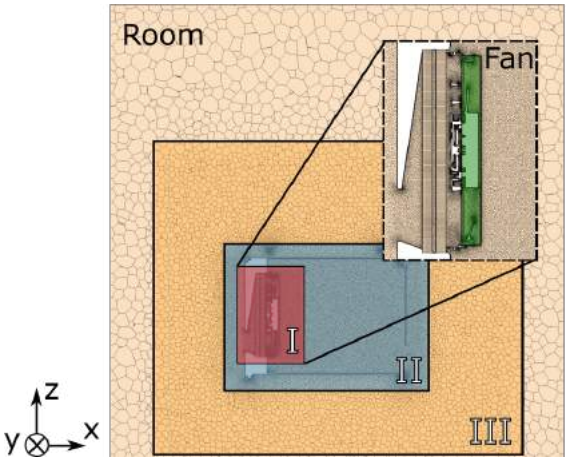

Figure 4.13: *Computational domain with mesh refinement regions for Fan A in the Stage II BEV set-up.*

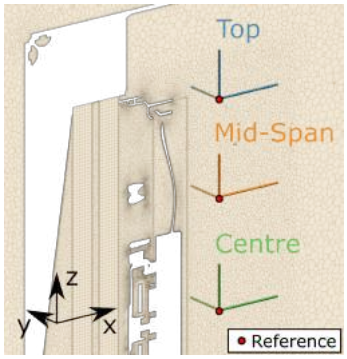

(a) *Line probes used for the two-point correlation analysis.*

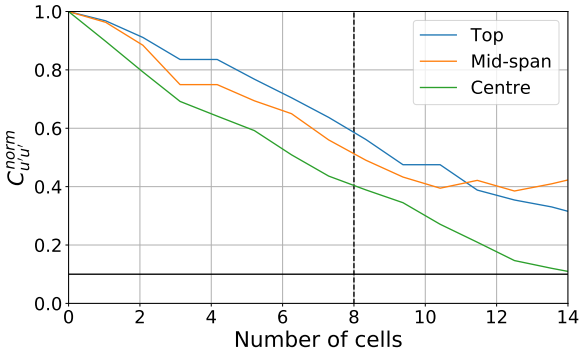

(b) *Normalised two-point correlation factor for the axial velocity component (x-direction).*

Figure 4.14: *Normalised two-point correlation.*

The simulations are started from a converged steady-state solution that was done using the MRF fan model, and are run with the DDES Elliptic blending k-ε model. The fan rotation was modelled with the RBM approach at the respective maximum rotational rate (2400 rpm (A)/ 2800 rpm (B)). With the conservative approach of allowing a rotation of 1 deg per time step, this resulted in a time step size of 6.94×10^{-5} s (A) and 5.95×10^{-5} s (B), respectively. This time step was reached after a transitional period of 0.5 s where the time step size was successively decreased starting from 10 deg per time step. The simulations were run at the lowest time step for 0.1 s before starting the averaging of the flow field over 20 revolutions. This yields a CFL number <1 in the majority of cells. Larger CFL numbers of up to 20 can be observed around the fan blades due to higher velocities, and the finer cell resolution that was employed in order to accurately capture the blade curvature.

A sensitivity study on the mesh resolution, time step size, averaging period and turbulence model has been performed and is described in Paper IV.

4.3.2 Results

The results are presented by comparing the projected velocity vectors for the experiments and simulations in the vertical centreline 0.05 m downstream of the respective fan motor. For selected configurations, a comparison of the flow field in a wake plane at the same distance from the fan motor is performed additionally. The experimental data was acquired according to the procedure described in Section 4.2. As the influence of the different components on the flow physics was discussed in detail in the previous section on the base of the measurements, the following section will focus on the ability of the simulation methods to capture these physics and discuss differences to the experimental data.

Stage I – Isolated fan

The first configurations consist of only the fan in the testrig, without any airguides, radiator cores or downstream blockages. In Figure 4.15, the predicted and measured flow field in the vertical centreline is presented. An axisymmetric flow behaviour can be noted for both fans, which is reasonable, due to the symmetry of the test rig. For Fan A, the numerical results show a strong axial flow over the complete blade span, while the experimental data shows a pronounced radial flow. The slightly reversed flow in the hub region is accurately captured. For Fan B, the numerical and experimental data agree well, showing an axial flow in the centreline with the velocity vectors being marginally tilted towards the axis of rotation.

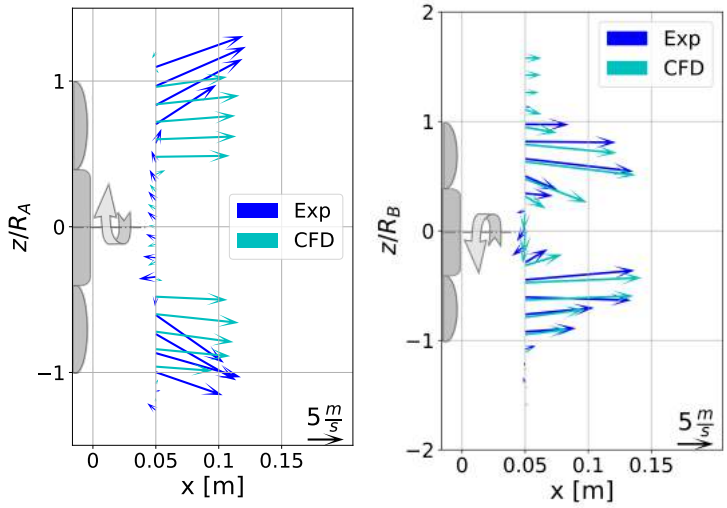

(a) *Fan A* (b) *Fan B*

Figure 4.15: *Projected velocity vectors in the centreline for the isolated fan set-ups.*

Stage II – Front openings

Figure 4.16 shows the velocity profiles in the centreline for Fan A in the BEV and HEV front without a downstream blockage. It can clearly be seen that introducing the radiator cores upstream of the fan notably reduces the velocity magnitude in the tip region. In addition, the flow has become more radial in comparison to the configuration with the isolated fan. The prediction of the flow field in CFD is closer to the experimental data than for the isolated fan. For both the BEV and HEV front design, the degree of radiality of the flow is approximately captured, even though the peak velocities are located closer to the hub than in the experiments.

A comparison of the numerical and experimental results in the wake plane at $x = 0.05\,\text{m}$ (Figure 4.17) confirms the observations made for the velocity profile in the centreline. For both fronts the overall velocity magnitude is lower in the simulations than in the experimental data and the peak velocities are found closer to the hub. Splitting the velocity magnitude into the axial, radial and tangential component showed, that all components are equally affected. However, looking at the vector fields projected onto the wake plane, many similarities are found between the CFD results and the measurements. Furthermore, the effect of the additional front grille opening in the HEV configuration is seen by the higher velocity magnitude around the upper tip region compared to the BEV set-up.

The velocity profiles along the centreline for Fan B are presented in Figure 4.18. Close agreement can be found in the lower tip region and hub area for both front designs. In the upper tip region, some differences can be noted. However, these differences are small and do not show systematic errors as were observed for Fan A.

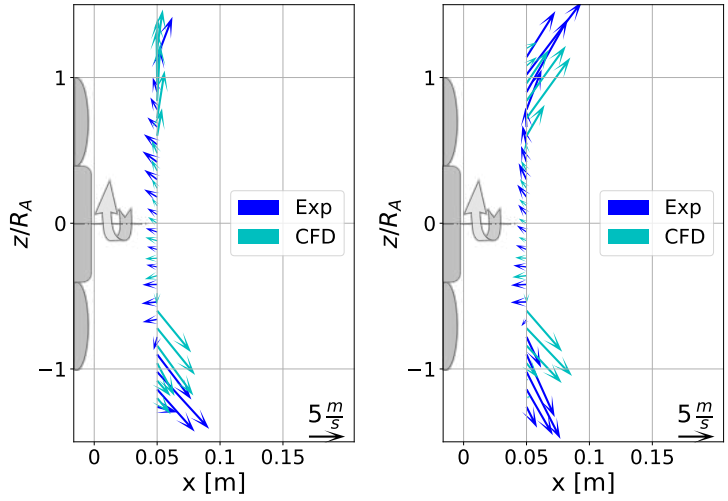

(a) *BEV* (b) *HEV*

Figure 4.16: *Fan A – projected velocity vectors along the vertical centreline without downstream blockage.*

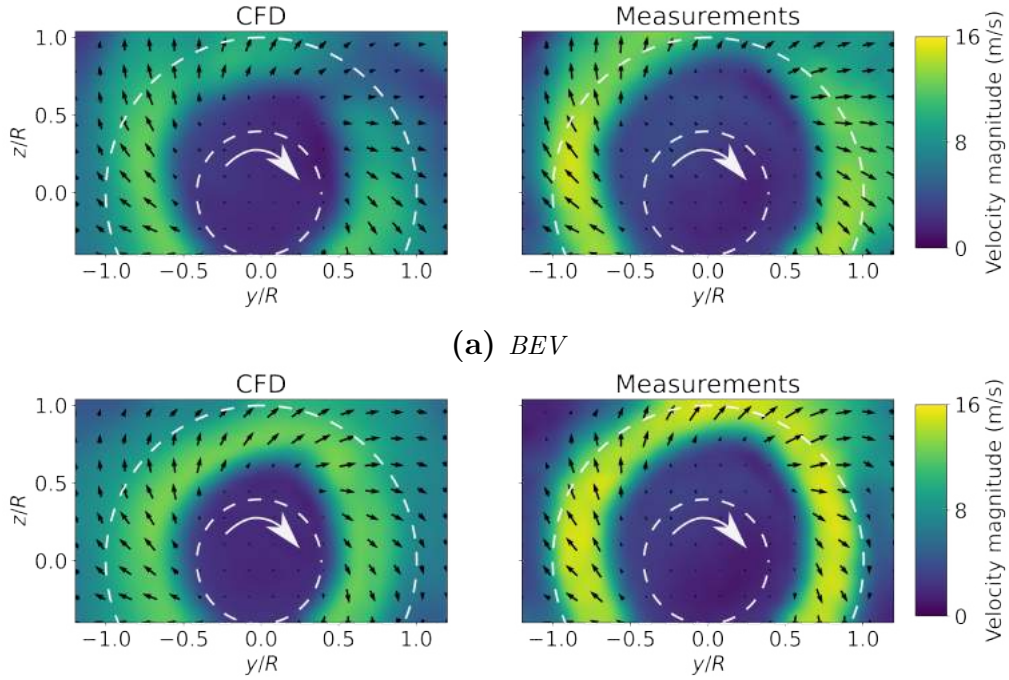

(a) *BEV*

(b) *HEV*

Figure 4.17: *Velocity field in the wake plane at $x = 0.05\,m$ for Fan A in the BEV and HEV configuration without a downstream blockage.*

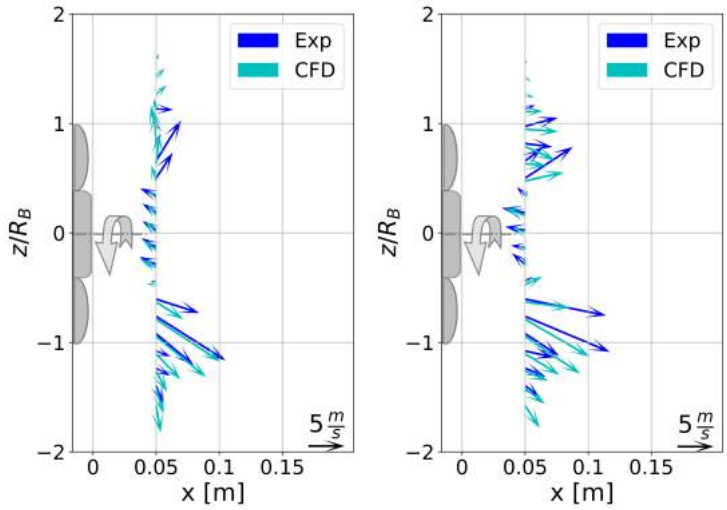

(a) *BEV* **(b)** *HEV*

Figure 4.18: *Fan B – projected velocity vectors along the vertical centreline without downstream blockage (Stage II).*

Stage III – Complete set-up

Including a symmetric blockage in the test section downstream of Fan A resulted in an increased axial flow in the upper and lower tip regions for both fronts (see Figure 4.19). Similar to the previously studied cases, the CFD simulations show the peak velocities closer to the axis of rotation. In the HEV configuration (Figure 4.19b), the predicted flow field in the hub region agrees well with the experimental results. The trend of the flow field is better captured in the upper tip region than in the lower one. In the set-up with the BEV front (see Figure 4.19a) the flow behaviour in the lower tip region is reasonably well captured, while the flow in the upper tip region is noticeable under-predicted. At the same time, an increased reversed flow in the hub region occurs in the flow simulations.

Figure 4.20 shows the comparison of the numerical and experimental results in the wake plane of the configurations with a blockage downstream of Fan A. Similar to the cases with an empty test section, the overall velocity magnitude in CFD is lower than in the experiments, but the trend of the predicted velocity vectors in the y-z-plane agrees well with the measurement data. In addition, the simulations also manage to capture the effect from the upper grille opening in the HEV set-up, which moves the centre of rotation of the swirling flow closer to the fan axis, while in the BEV configuration it is located at approximately the edge of the hub.

For Fan B, the velocity vectors along the vertical centreline in the configurations with a downstream blockage are presented in Figure 4.21. The effect from merely

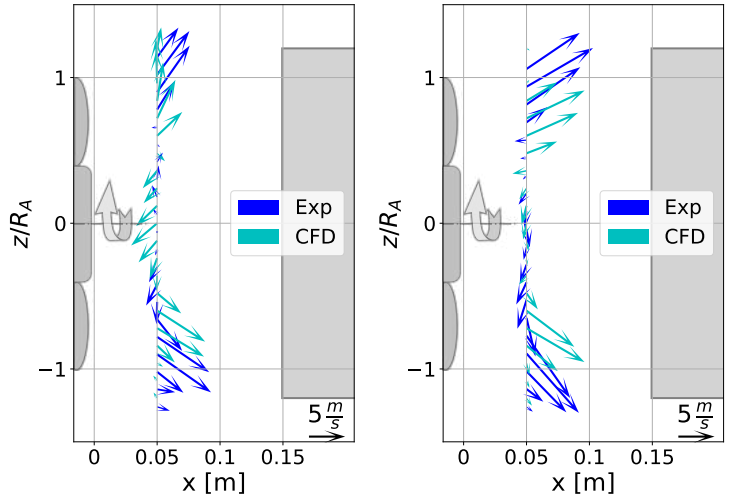

(a) *BEV* (b) *HEV*

Figure 4.19: *Fan A – projected velocity vectors along the vertical centreline with downstream blockage.*

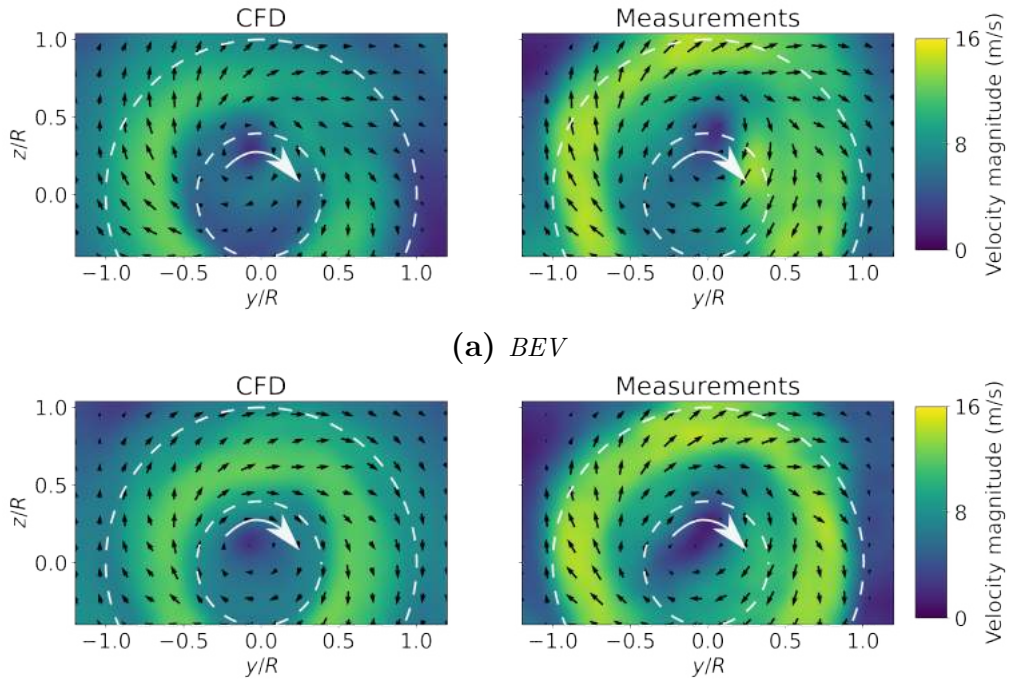

(a) *BEV*

(b) *HEV*

Figure 4.20: *Velocity field in the wake plane at $x = 0.05\,m$ for Fan A in the BEV and HEV configuration with a symmetric blockage downstream of the fan.*

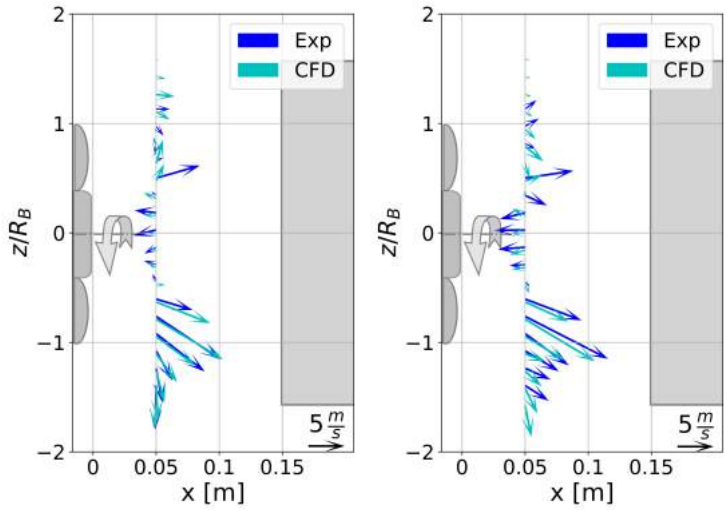

(a) *BEV* **(b)** *HEV*

Figure 4.21: *Fan B – projected velocity vectors along the vertical centreline with a downstream blockage.*

having a lower grille opening are less pronounced than in the configurations with an empty test section. In the set-ups that include the blockage, the velocity vectors in the upper tip region are similarly low in the BEV and HEV configuration. This is likely due to the smaller diameter of Fan B in comparison to Fan A, which places the tip region in the swirl that occurred in the Fan A configuration with blockage. The lower tip region is less affected due to the outlet opening in the lower rear of the rig.

4.3.3 Discussion

Since the numerical and experimental methodology have been identical for both fan set-ups, the reason for the different quality of the results is likely founded in the two fans' parameters. Figure 4.22 shows the time-averages streamlines of the velocity in the centreplane of the rig for the different fans in the BEV configuration with and without blockage. As the observed deviations in the velocity profiles were consistent between the different configurations with and without downstream blockage, an influence from the recirculating flow in the test section is considered unlikely, but could be taken into consideration for future studies.

Other possible influencing factors concern the geometry of Fan A and B. Firstly, the diameter for Fan A is larger than for Fan B, which reduces the distance from the fan tips to the walls notably. This could lead to an unwanted interference

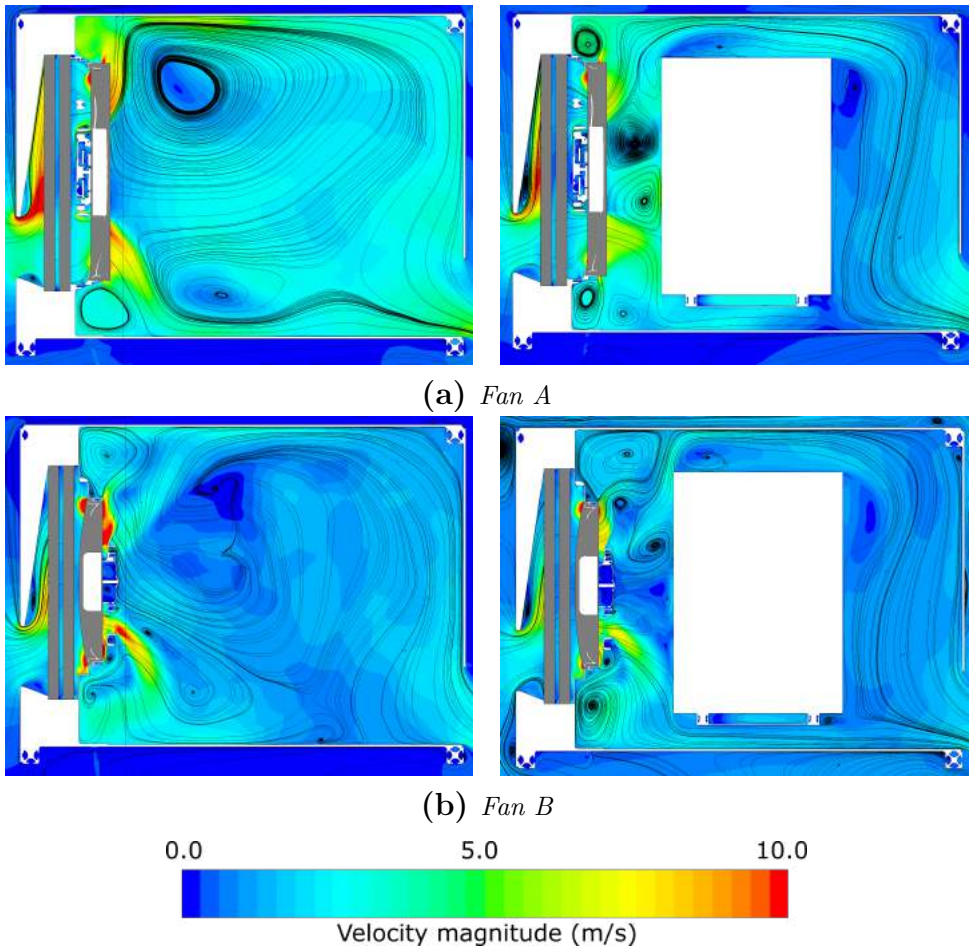

(a) *Fan A*

(b) *Fan B*

Figure 4.22: *Streamlines in the test section for Stage II and III.*

between the high velocity flow close to the outer diameter and the stationary walls. Secondly, the struts of Fan A are forming a fine net that is located upstream of the rotor, while Fan B has fewer but broader struts located downstream of the fan. It is possible, that the flow field downstream of Fan B is, therefore, dominated by the wake of these struts, or that the undisturbed inflow to Fan B yields a better performance of the simulations. Further investigations will be necessary to improve the understanding of these influencing factors for underhood simulations.

5 | Conclusions

The aim of this project has been to improve the understanding of the physics of underhood flow and assess the accuracy of current simulation methods to capture the occurring phenomena. This has been done by experimental and numerical studies on an isolated fans, as well as by placing them in a simplified underhood environment that was built as part of this project.

In a first step, the two most common fan modelling approaches, MRF and RBM, were evaluated and compared to measurement data. The results showed that the MRF model is unsuitable for predicting underhood flow, as the frozen rotor position produces an uneven flow distribution. Averaging multiple steady-state MRF simulations for different rotor positions resulted in a more uniform flow field, but it still showed differences to the results from applying the RBM method and experimental data. In a following numerical study, these differences could be related to the static pressure build-up from the fan struts downstream of the MRF interface, which affected the streamlines in the moving reference frame. Moreover, it was shown that when using the MRF method, an inhomogeneous temperature field experiences an unphysical rotation over the fan domain. In the RBM approach, the agreement with the time-averaged velocity measurements on an isolated fan was good.

In a second stage of the project, a simplified underhood environment was developed as a tool to improve understanding of underhood flow and obtain validation data for CFD. This rig could be modified in order to assess different front designs representative for electric vehicles as well as the effect of different downstream blockages. The experiments showed a clear impact from the different front opening designs on the flow downstream of the fan. However, this impact became less noticeable when introducing downstream obstacles. The lateral and axial distance between the blockages and the fan had close to no impact on the flow field within the investigated range. Numerical simulations of the same front configurations, with and without a downstream blockage, were performed for two different fans. The employed methodology used the RBM method for resolving the fan rotation and the DDES Elliptic Blending k-ε turbulence model. A sensitivity study proved the ro-

bustness of the set-up with respect to mesh settings, time step size, averaging period and turbulence model. Still, the agreement between the simulations and measurements varied for the two fans. While the simulations for one fan showed good agreement with the experimental data, the ones for the other fan under-predicted the overall velocity magnitude and predicted the location of the peak velocities closer to the hub than the measurement showed. However, the general flow behaviour was still captured. Several aspects were identified that differ between the two fans and could be responsible for the varying performance of the simulations. These aspects concerned mainly geometric features, such as the distance between the outer fan diameter and the peripheral walls and the fan struts.

For future works, it could be of interest to further investigate which fan characteristics play an important role when predicting the velocity field downstream of the fan in CFD. Once these influencing factors are better understood, the complexity of the simplified underhood environment could be increased by including multiple smaller or more detailed geometries, and study the flow distribution around these components. In addition, flow features other than the averaged velocity field should be studied to further increase the knowledge about how the flow field is affected by different installations. As the overall objective is to shape a thermally efficient environment and reduce unwanted heat-losses, future investigations should eventually also include thermal sources to study the heat transfer in the underhood, for example to and from coolant hoses.

6 | Summary of appended papers

Paper I

Validation of Different Fan Modelling Techniques in Computational Fluid Dynamics

In this paper, three different approaches to numerically model the rotation of an axial cooling fan were investigated. The results were compared to experimental data that was obtained by using Laser Doppler Anemomentry (LDA). The different modelling methods were the steady-state Multiple Reference Frame (MRF), a modification of the MRF approach called average MRF (avgMRF) and the unsteady Rigid Body Motion (RBM), or Sliding Mesh, approach.

The study showed that the standard MRF model is not able to replicate the measured flow field due to the frozen rotor position. In the avgMRF method the flow field was averaged over different rotor positions, which resulted in a better agreement with the measurement data. A parameter study was performed, showing that the impact from the frozen rotor blade is no longer noticeable when using more than three blade positions. However, the MRF based approaches showed substantial differences in the axial flow field in the proximity of the struts. Here, only the RBM approach managed to capture the flow behaviour that was observed in the experimental results.

Paper II

Evaluation of the Multiple Reference Approach for the Modelling of an Axial Cooling Fan

As the MRF approach is still widely used due to its computational efficiency, this paper studied the transport mechanisms through the fan region when using this method. The two areas of interest were the transport of an inhomogeneous temperature field, and the effect of differently shaped stationary structures close to the interfaces. RBM simulations were used as a reference.

This paper showed that the temperature field experiences an unphysical rotation when utilising the MRF approach. The degree of rotation is depended on the length of the MRF domain and the fan speed. The cause for the rotation is that the temperature field is transported using the relative streamlines, which ensures that the streamlines do not collide with the stationary blades and information gets lost. Geometrical structures upstream of the MRF region have close to no effect on the downstream flow field. If a component is located in proximity to the downstream interface, the static pressure build-up in front of the structure can extend into the MRF domain and affect the velocity field in the rotating reference frame. This effect caused the deviations in the flow field around the stationary structures downstream of the fan region, when comparing the results from MRF to RBM simulations and the experimental results reported in Paper I.

Paper III

Experimental investigation of the air flow in a simplified underhood environment

For Paper III, a simplified underhood testbed was designed and built in order to study the effects of different geometric components on the flow field downstream of the cooling fan. This paper contains a detailed description of the set-up and experimental results. The front could be varied between a typical BEV and HEV configuration. In addition, two different large obstructions could be placed in the test section, and their position could be varied in longitudinal and lateral direction.

It was shown that the lack of an upper grille opening in the BEV configuration without a downstream blockage notable reduced the velocity magnitude in upper part of the underhood. When a downstream obstruction was present, this effect was less pronounced. The longitudinal and lateral position of the blockages relative to the fan had less of an impact on the flow field than the shape of the obstacle itself.

Paper IV

Numerical investigation of the air flow in a simplified underhood environment

In this paper, numerical simulations were performed on the simplified underhood geometry presented in Paper III. Two different production fans were included, and the installation effect of different up- and downstream configurations was investigated. The simulations were validated against experimental results.

In a first step, the robustness of the numerical methodology was tested with respect to different mesh resolutions, time step sizes, averaging periods and turbulence models. The variation resulted in small differences, but did not have a large impact on the flow topology. Applying this methodology to the two fans yielded a varying quality of results in comparison to the measurements. For the first fan, the general trend in the flow field was captured, but the peak velocities in the simulations were found closer to the centre of rotation than in the measurements. For the second fan, the flow field obtained from the CFD simulations was in good agreement to the measurements for all tested configurations. As the numerical method was identical for both fans, different geometrical properties were discussed as a possible influence factor on the performance.

Appendix

Simplified underhood geometry

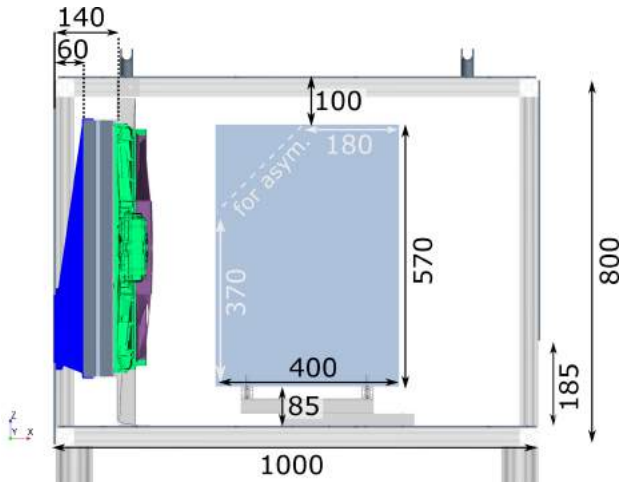

Figure A.1: *Additional information about the dimensions in the test rig (in mm).*

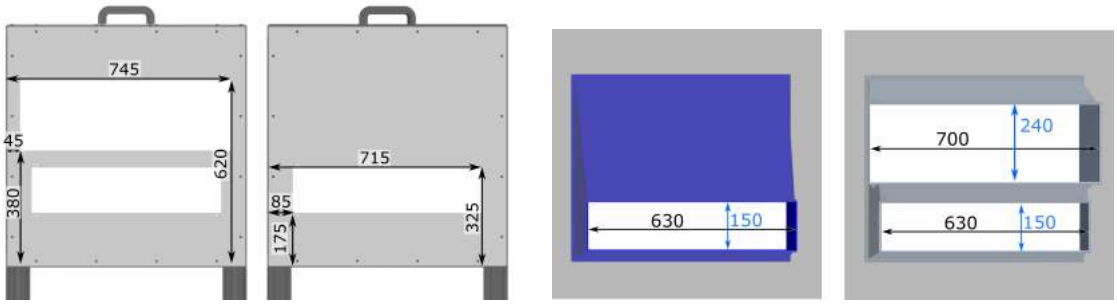

Figure A.2: *Placement and dimensions of the front openings (im mm).*

A.1 Fan parameters

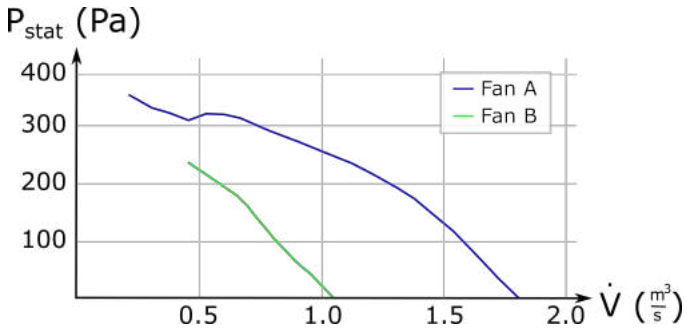

Figure A.3: *Fan performance curves of the utilised fans.*

Table A.1: *Fan specifications.*

	Fan A	**Fan B**
Manufacturer	brose	Johnson Electric
Power [W]	600	390
Outer diameter [mm]	500	380
Hub diameter [mm]	200	140
No. Blades	7	8
Max. speed [rpm]	2400	2800

A.2 Mesh parameters

Table A.2: *Mesh parameters for the MWT set-up (see Section 3.1.2).*

Parameter	**Mesh**
Base size Air region	16 mm
Base size Fan	2 mm
Prism Layers Fan	10
Prism Layer Thickness Fan	1 mm

Note: In the most recent software version that was available at the time of the study, it was not possible to use refinement regions for polyhedral meshes. Therefore the cell size was adjusted by setting a surface element size of 2 mm on the shroud and interfaces to the fan region.

Table A.3: *Mesh parameters for the pipe set-up (see Section 3.2.1).*

Parameter	Mesh
Base size pipe	12 mm
Ref. I	5 mm
Ref. II	10 mm
Prism Layers Pipe	5
Prism Layer Thickness Pipe	2.5 mm
Base size Fan	4 mm
Prism Layers Fan	10
Prism Layer Thickness Fan	1 mm
Radiator	5 mm

Table A.4: *Mesh parameters with respect to areas shown in Figure 4.13*

Region	Mesh
Room	32 mm
Ref. I	4 mm
Ref. II	8 mm
Ref III	16 mm
Fan	4 mm
Prism Layers Fan	10
Prism Layer Thickness Fan	1 mm
Radiator	4 mm

Bibliography

[1] "New registrations of passenger cars by fuel (2006 - 2021)," tech. rep., Statistiska Centralbyrån (SCB), 2021.

[2] W. H. Hucho, *Aerodynamics of road vehicles*. SAE International, 5th ed., 2015.

[3] R. Franzke, R. Svensson, T. Thiringer, E. Willeson, E. Grunditz, and A. Broniewicz, "Measurements and CFD modeling of temperatures in the engine compartment of a hybrid electric vehicle," *2017 IEEE Vehicle Power and Propulsion Conference, VPPC 2017 - Proceedings*, 2017.

[4] A. Cogotti and H. Berneburg, "Engine compartment airflow investigations using a Laser-Doppler-Velocimeter," *SAE Technical Paper 910308*, 1991.

[5] H. Berneburg and A. Cogotti, "Development and use of LDV and other airflow measurement techniques as a basis for the improvement of numerical simulation of engine compartment air flows," *SAE Technical Paper 930294*, 1993.

[6] J. E. Williams, "Water flow simulation of automotive underhood airflow phenomena," *SAE Technical Paper 910307*, 1991.

[7] J. F. Foss, J. K. Schwannecke, A. R. Lawrenz, M. W. Mets, S. C. Treat, and M. D. Dusel, "The thermal transient anemometer," *Measurement Science and Technology*, vol. 15, 2004.

[8] E. Y. Ng, S. Watkins, P. W. Johnson, and L. Mole, "Measuring local time-averaged airflow velocity through an automotive heat exchanger," *Proceedings of the 14th Australasian Fluid Mechanics Conference*, 2001.

[9] M. Khaled, F. Mangi, H. E. Hage, F. Harambat, and H. Peerhossaini, "Fan air flow analysis and heat transfer enhancement of vehicle underhood cooling system - Towards a new control approach for fuel consumption reduction," *Applied Energy*, vol. 91, pp. 439–450, 2012.

[10] M. Khaled, M. Gad El Rab, F. Hachem, H. Elhage, A. Elmarakbi, F. Harambat, and F. Peerhossani, "Experimental study of the flow induced by a vehicle fan and the effect of engine blockage in a simplified model," *International Journal of Automotive Technology*, vol. 13, no. 2, pp. 293–300, 2016.

[11] J. Faraj, E. Harika, M. Ramadan, S. Ali, F. Harambat, and M. Khaled, "Effect of underhood architecture on aerodynamic drag — suggestion of new concepts for fuel consumption reduction," *International Journal of Automotive Technology*, vol. 21, no. 3, pp. 633–640, 2020.

[12] M. Karlsson and S. Etemad, "Installation effects on the flow generated noise from automotive electrical cooling fans," *SAE Technical Paper 2020-01-1516*, 2020.

[13] M. Franchetta, K. O. Suen, P. A. Williams, and T. G. Bancroft, "Investigation into natural convection in an underhood model under heat soak condition," *SAE Technical Papers 2005-01-1384*, 2005.

[14] D. Mukutmoni, A. Alajbegovic, and J. Han, "Numerical simulation of transient thermal convection of a full vehicle," *SAE Technical Paper 2011-01-0645*, 2011.

[15] B. Sweetman, I. Schmitz, B. Hupertz, N. Shaw, and J. Goldstein, "Experimental and numerical investigation of vehicle drive and thermal soak conditions in a simplified engine bay," *SAE International Journal of Passenger Cars - Mechanical Systems*, vol. 10, no. 2, pp. 433–445, 2017.

[16] F. Zenger, C. Junger, M. Kaltenbacher, and S. Becker, "A benchmark case for aerodynamics and aeroacoustics of a low pressure axial fan," *SAE Technical Paper 2016-01-1805*, 2016.

[17] A. Rynell, *An experimental and numerical study of an automotive cooling module*. PhD Thesis, KTH Royal Institute of Technology, 2017.

[18] S. Wen, Y. Hao, Z. Zhang, and Y. Wang, "Experimental study on the effect of different components collocations on flow of automotive cooling fan," *Proceedings of the Institution of Mechanical Engineers, Part D: Journal of Automobile Engineering*, vol. 234, pp. 270–282, 2020.

[19] I. Kohri and Y. Kobayashi, "Prediction of the performance of the engine cooling fan with CFD simulation," *SAE International Journal of Passenger Cars - Mechanical Systems*, vol. 3, no. 1, pp. 508–522, 2010.

[20] S. Moreau and E. Bennett, "Improvement of fan design using CFD," *SAE Technical Paper 970934*, 1997.

[21] J. Foss, D. Neal, M. Henner, and S. Moreau, "Evaluating CFD models of axial fans by comparisons with phase-averaged experimental data," *SAE Technical Paper 2001-01-1701*, 2001.

[22] M. Henner, S. Moreau, D. Neal, and J. D. Laborderie, "Validation of 3D rotor-stator URANS in automotive engine cooling fan systems," in *Proceedings of the 8th International Symposium on Experimental and Computational Aero-thermodynamics of Internal Flows*, (Lyon), 2007.

[23] P. Gullberg, L. Löfdahl, S. Adelman, and P. Nilsson, "A correction method for stationary fan CFD MRF models," *SAE Technical Paper 2009-01-0178*, 2009.

[24] P. Gullberg, L. Löfdahl, S. Adelman, and P. Nilsson, "An investigation and correction method of stationary fan CFD MRF simulations," *SAE Technical Paper 2009-01-3067*, 2009.

[25] P. Gullberg, *Optimisation of the flow process in engine bays - 3D modelling of cooling airflow*. PhD Thesis, Chalmers University of Technology, 2011.

[26] P. Gullberg, L. Löfdahl, P. Nilsson, and S. Adelman, "Continued study of the error and consistency of fan CFD MRF models," *SAE Technical Paper 2010-01-0553*, 2010.

[27] Y. Kobayashi and I. Kohri, "Study of influence of MRF method on the prediction of the engine cooling fan performance," *SAE Technical Paper 2011-01-0648*, 2011.

[28] P. Gullberg and L. Löfdahl, "Fan modelling in CFD using MRF model for under hood purposes," in *Proceedings of the ASME-JSME-KSME Joint Fluids Engineering Conference 2011*, (Hamamatsu), 2011.

[29] P. Gullberg, L. Löfdahl, and P. Nilsson, "Cooling airflow system modeling in CFD using assumption of stationary flow," *SAE Technical Paper 2011-01-2182*, 2011.

[30] M. Riesterer, *Numerische Abbildung des Wärmetransports durch einen PKW-Axiallüfter [Numerical simultion of heat-transfer through an automotive axial cooling fan.]*. PhD Thesis, Karlruher Intitute of Technology, 2016.

[31] N. L. Gifford, E. Savory, and R. J. Martinuzzi, "Experimental study of automotive cooling fan aerodynamics," *SAE Technical Paper 2007-01-1525*, 2007.

[32] Siemens, "Simcenter StarCCM+ Documentation," 2021.

[33] H. Versteeg and W. Malalasekera, *An Introduction to Computational Fluid Dynamics : The Finite Volume Method*. Harlow: Pearson Prentice Hall, 2 ed., 2007.

[34] B. Minovski, L. Löfdahl, and P. Gullberg, "Numerical investigation of natural convection in a simplified engine bay," *SAE Technical Paper 2016-01-1683*, 2016.

[35] P. Ekman, J. Venning, T. Virdung, and M. Karlsson, "Importance of subgrid scale modeling for accurate aerodynamic simulations," *Journal of Fluids Engineering*, vol. 143, no. 1, 2020.

[36] C.-M. Jang, M. Furukawa, and M. Inoue, "Analysis of vortical flow field in a propeller fan by LDV Measurements and LES—Part I: Three-dimensional vortical flow structures ," *Journal of Fluids Engineering*, vol. 123, no. 4, pp. 748–754, 2001.

[37] D. Borello, A. Corsini, G. Delibra, M. Fiorito, and A. G. Sheard, "Large-Eddy Simulation of a tunnel ventilation fan," *Journal of Fluids Engineering*, vol. 135, no. 7, 2013. 071102.

[38] A. Pogorelov, M. Meinke, and W. Schröder, "Large-Eddy Simulation of the flow field in a rotating axial fan," *New Results in Numerical and Experimental Fluid Mechanics*, 2016.

[39] S. M. Lim, A. Dahlkild, and M. Mihaescu, "Aerothermodynamics and exergy analysis of a turbocharger radial turbine integrated with exhaust manifold," in *Proceedings of the 13th International Conference on Turbochargers and Turbocharging*, (London), KTH, Fluid Physics, 2018.

[40] A. Rynell, G. Efraimsson, M. Chevalier, and M. Abom, "Inclusion of upstream turbulent inflow statistics to numerically acquire proper fan noise characteristics," *SAE Technical Paper 2016-01-1811*, 2016.

[41] P. R. Allmaras and S. R. Spalart, "A one-equation turbulence model for aerodynamic flows," *La recherche aerospatiale*, no. 1, pp. 5–21, 1994.

[42] F. R. Menter, "Improved two-equation k-omega turbulence models for aerodynamic flows," tech. rep., NASA STI/Recon Technical Report N, 1992.

[43] D. C. Wilcox, *Turbulence modeling for CFD*. DCW Industries, 1998.

[44] S. B. Pope, "Ten questions concerning the large-eddy simulation of turbulent flows," *New Journal of Physics*, vol. 6, 2004.

[45] L. Davidson, "Large Eddy Simulations: How to evaluate resolution," *International Journal of Heat and Fluid Flow*, vol. 30, no. 5, pp. 1016–1025, 2009.

[46] L. Henriksson, *Performance of compact heat exchanger in non-perpendicular cooling airflows*. PhD Thesis, Chalmers University of Technology, 2015.

[47] A. Rynell, "A numerical investigaton of aerodynamic and acoustic installation effects caused by an upstream automotive radiator." QC 20160104.

[48] T. Kuthada, F. Wittmeier, B. Bock, C. Schoenleber, and A. Link, "The effects of cooling air on the flow field around a vehicle," *SAE International Journal of Passenger Cars - Mechanical Systems*, vol. 9, no. 2, pp. 723–732, 2016.

[49] M. B. Dogruoz and G. Shankaran, "Computations with the Multiple Reference Frame technique: Flow and temperature fields downstream of an axial fan," *Numerical Heat Transfer; Part A: Applications*, vol. 71, no. 5, pp. 488–510, 2017.

[50] A. Wang, Z. Xiao, and H. Ghazialam, "Evaluation of the Multiple Reference Frame (MRF) model in a truck fan simulation," *SAE Technical Paper 2005-01-2067*, 2005.

[51] W. Peng, G. Li, J. Geng, and W. Yan, "A strategy for the partition of MRF zones in axial fan simulation," *International Journal of Ventilation*, vol. 18, no. 1, pp. 64–78, 2019.

[52] P. Gullberg and A. Tavernier, "Modeling of closed fans using CFD and steady state assumption of fluid flow," *SAE Technical Paper 2014-01-2344*, 2014.

[53] E. Baniasadi, M. Aydin, I. Dincer, and G. Naterer, "Computational aerodynamic study of automotive cooling fan in blocked conditions," *Engineering Applications of Computational Fluid Mechanics*, vol. 7, no. 1, pp. 66–73, 2013.

[54] İlhan Öztürk, C. Çetin, and M. M. Yavuz, "Effect of fan and shroud configurations on underhood flow characteristics of an agricultural tractor," *Engineering Applications of Computational Fluid Mechanics*, vol. 13, no. 1, pp. 506–518, 2019.

[55] Dantec Dynamics A/S, "BSA Flow Software User Guide," 2019.

[56] T. Anthoine, T. Arts, H. Boerrigter, J.-M. Buchlin, M. Carbonaro, G. Degrez, R. Dénos, D. Fletcher, D. Olivari, M. Riethmuller, and R. Van den Braembussche, *Measurement Techniques in Fluid Dynamics - An Introduction*. 2009.

[57] R. Franzke, *CFD modelling of axial fans for thermal management applications*. Licentiate thesis, Chalmers University of Technology, 2019.

[58] S. Bell, "The beginner's guide to uncertainty of measurement," tech. rep., National Physical Laboratory, 2013.